An integrated framework for 3D time history analysis of steel special moment-resisting frame buildings under sequential flood and earthquake hazards

Samadian, Delbaz; Eslamnia, Hadi; Muhit, Imrose B.; Pregnolato, Maria; Dawood, Nashwan

DOI
10.1080/15732479.2025.2591815

Publication date
2025

Document Version
Final published version

Published in
Structure and Infrastructure Engineering

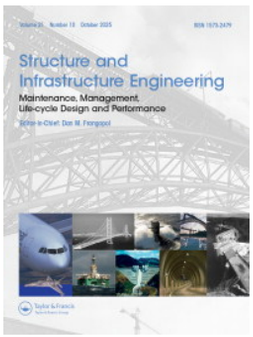

Taylor & Francis
Taylor & Francis Group

Structure and Infrastructure Engineering
Maintenance, Management, Life-Cycle Design and Performance

ISSN: 1573-2479 (Print) 1744-8980 (Online) Journal homepage: www.tandfonline.com/journals/nsie20

An integrated framework for 3D time history analysis of steel special moment-resisting frame buildings under sequential flood and earthquake hazards

Delbaz Samadian , Hadi Eslamnia , Imrose B. Muhit , Maria Pregnolato & Nashwan Dawood

To cite this article: Delbaz Samadian , Hadi Eslamnia , Imrose B. Muhit , Maria Pregnolato & Nashwan Dawood (21 Nov 2025): An integrated framework for 3D time history analysis of steel special moment-resisting frame buildings under sequential flood and earthquake hazards, Structure and Infrastructure Engineering, DOI: 10.1080/15732479.2025.2591815

To link to this article: https://doi.org/10.1080/15732479.2025.2591815

STRUCTURE AND INFRASTRUCTURE ENGINEERING
https://doi.org/10.1080/15732479.2025.2591815

An integrated framework for 3D time history analysis of steel special moment-resisting frame buildings under sequential flood and earthquake hazards

Delbaz Samadian[a], Hadi Eslamnia[b], Imrose B. Muhit[a], Maria Pregnolato[c] and Nashwan Dawood[a]

[a]School of Computing, Engineering and Digital Technologies, Teesside University, Middlesbrough, UK; [b]Independent Researcher in Earthquake Engineering, Istanbul, Turkey; [c]Department of Hydraulic Engineering, Delft University of Technology, Delft, Netherlands

ABSTRACT

With climate change intensifying risks of extreme precipitation and riverine flooding, reassessing building resilience under multi-hazard scenarios, particularly those involving earthquakes, has become increasingly important. This study proposes an integrated framework for three-dimensional (3D) nonlinear time history analysis (NLTHA) to evaluate structural performance under sequential earthquake and flood events. By coupling advanced Computational Fluid Dynamics (CFD) simulations with earthquake engineering methods, the framework captures the time-dependent interaction of seismic and hydrodynamic forces. This overcomes limitations of previous research that relied on oversimplified flood-earthquake interaction models. The analysis focuses on steel special moment-resisting frame (SMRF) buildings in Los Angeles, California. Thirteen seismic hazard levels and four flood inundation depths are analysed, producing detailed engineering demand parameters (EDPs) for both earthquake-only and combined hazard scenarios. Structural vulnerability is evaluated through ductility and plastic hinge rotation in columns and beams. Results show flooding significantly amplifies EDPs, especially in lower stories and front-facing elements, emphasising the need to revise design and assessment strategies for buildings in flood-prone areas. Furthermore, vortex shedding and asymmetric water flow patterns around corners and side columns increase localised hydrodynamic pressures. This integrated approach provides engineers with a comprehensive framework for analysing structures to withstand future climate-driven multi-hazard events.

ARTICLE HISTORY
Received 12 May 2025
Accepted 25 August 2025

KEYWORDS
Climate change; earthquake; flooding; multi-hazard scenario; steel buildings; time history analysis

1. Introduction

Natural disasters disrupt livelihoods and infrastructure, necessitating proactive strategies to mitigate their impacts, particularly as global warming and climate change intensify these threats (World Economic Forum, 2023). Floods (riverine, coastal, flash) and earthquakes are among the most significant hazards, causing $20.37 billion and $17.62 billion in damages, respectively, in 2023 alone (Daniell & Armand, 2012; EM-DAT, 2024; Guha-Sapir et al., 2013; Jonkman et al., 2024; Jonkman & Vrijling, 2008; Samadian et al., 2019; Vanneste et al., 2018). Between 1975 and 2022, these hazards resulted in approximately 830,000 fatalities globally (Jonkman et al., 2024), highlighting the need for strategies to reduce vulnerability and enhance resilience. With their frequency and intensity projected to rise due to climate change, urbanisation, and population growth in vulnerable areas, understanding their impacts on critical structures is essential (Kreibich et al., 2022). In line with Global Target A of the Sendai Framework (UNDRR, 2015), structural engineers must develop robust assessment frameworks to enhance building resilience.

Recent research has focused on structural vulnerability to individual and combined hazards, particularly floods and earthquakes. Studies have assessed seismic impacts on key infrastructure, including schools (Soltani et al., 2023), bridges (Ghaffarpasand et al., 2024), hospitals (Liu et al., 2022), and heritage structures (Xu et al., 2024). For example, Soltani et al. (2023) analysed the seismic resilience index of concrete frame school buildings, providing insights into structural vulnerabilities. Ghaffarpasand et al. (2024) explored the seismic resilience of curved bridges by evaluating different retrofitting strategies using advanced computational methods. Liu et al. (2022) developed a probabilistic framework for assessing the seismic resilience of hospitals using Bayesian networks. Their approach established connections between the fragility of various wards and functional sections within a hospital, while also quantifying the interdependencies among non-structural components, enabling a more integrated and system-level evaluation of hospital performance under seismic events. Regarding heritage

CONTACT Imrose B. Muhit i.muhit@tees.ac.uk School of Computing, Engineering and Digital Technologies, Teesside University, Middlesbrough, TS1 3BX, UK

Supplemental data for this article is available online at https://doi.org/10.1080/15732479.2025.2591815

buildings, Xu et al. (2024) conducted a numerical study on historical masonry towers, calibrating their models with experimental data to estimate the damage index for wall components.

These works have identified critical vulnerabilities and proposed resilience indices or retrofitting strategies. Similarly, flood risk research has progressed, examining structural responses to dynamic loads (Asad et al., 2024; Lonetti & Maletta, 2018; Mazzorana et al., 2014; Milanesi et al., 2018), incorporating soil-structure interaction (SSI) (Mazzorana et al., 2014), and applying Computational Fluid Dynamics (CFD) to simulate flood impacts (Fairuz et al., 2020; Le et al., 2024; Motley et al., 2016; Viccione & Izzo, 2022). Lonetti and Maletta (2018) analysed dynamic impacts on masonry buildings during floods, while Asad et al. (2024) examined the out-of-plane failure of masonry walls in flash floods. Mazzorana et al. (2014) incorporated SSI in their models to simulate building behaviour under flood loads, defining ultimate failure or significant deformation as critical states. Milanesi et al. (2018) proposed a simplified conceptual model for assessing masonry structures' flood vulnerability using minimal input data.

Viccione and Izzo (2022) investigated the role of three-dimensional (3D) CFD in assessing urban flood forces on buildings in Italy, highlighting a significant correlation between urban flooding and topographical features. Le et al. (2024) examined the response of a reinforced concrete (RC) frame building under various flood scenarios using a coupled CFD-Finite Element Method (FEM) model. Their findings indicated that flow-structure interaction during the initial phase generates significantly greater impact loads than those observed during the steady state. Fairuz et al. (2020) evaluated the performance of different building configurations subjected to flooding through CFD analysis, concluding that buildings with smaller window sizes exhibit reduced vulnerability, while window orientation also influences structural susceptibility. Additionally, Motley et al. (2016) utilised 3D CFD to assess the resilience of skewed bridges under tsunami forces, revealing that the skewed design can amplify the steady-state fluid forces acting on the bridge deck.

While some studies address combined hazards such as earthquakes and tsunamis (Attary et al., 2021; Harati & van de Lindt, 2024), research on earthquake-flood interactions remains limited. For example, Korswagen et al. (2019) developed a probabilistic framework for evaluating structural damage from earthquakes and floods, focusing on masonry structures. Likewise, Vatteri et al. (2022) introduced a Bayesian Network to analyse masonry school buildings' performance under combined hazards, discussing recovery strategies. Ge et al. (2023) assessed the seismic vulnerability of ageing reinforced concrete bridges under climate change, corrosion, and seismic activity. Similarly, Argyroudis and Mitoulis (2021) investigated bridge failures due to the dual impacts of floods and earthquakes. Also, Dong et al. (2022) examined flood scouring effects on masonry structures, identifying a critical scour depth beyond which structural fragility significantly increases. In a related contribution, Prendergast et al. (2018) examined the performance of bridges under combined flooding and seismic actions, emphasising the complex interplay between scour-induced foundation stiffness loss and seismic forces. They demonstrated how scour can both increase flexibility, potentially reducing inertial seismic forces, and lead to detrimental secondary effects such as pier tilting and crack propagation, thereby increasing vulnerability. The study further highlighted the promise of vibration-based structural health monitoring (SHM) methods as a practical solution for detecting damage under multi-hazard conditions.

2. Methodology and research gap

This study introduces a novel and comprehensive framework that integrates 3D CFD and 3D nonlinear finite element (FE) analysis to assess the structural performance of buildings under sequential flood and earthquake hazards. Unlike previous research, which typically applies simplified or decoupled force-based methods such as equivalent static loads or pushover analysis (Dong & Frangopol, 2017; Petrone et al., 2020; Tagle et al., 2021), the proposed approach is the first to implement nonlinear time history analysis (NLTHA) for structures subjected to combined, time-dependent seismic and hydrodynamic forces. A key innovation of this framework is its ability to carry forward seismic damage, including strength and stiffness degradation, into the flood loading phase, rather than treating the hazards as independent events. This approach allows for the simulation of progressive damage accumulation, providing a more realistic representation of structural performance under complex, sequential hazard scenarios. High-fidelity CFD simulations are used to generate transient hydrodynamic loads, which are applied directly to the already-damaged structure.

The research also introduces a practical methodology to map detailed CFD-derived flood forces (including time-varying drag, lift, and overturning moments) onto FE models at the element level, using a custom-developed Python interface. In addition to the multi-hazard integration, the study proposes a new 3D modelling approach for steel special moment-resisting frame (SMRF) buildings, which enables significantly lower computational cost for NLTHA without compromising accuracy. Furthermore, the framework includes a robust vulnerability assessment based on both global engineering demand parameters (EDPs) and local plastic hinge rotations, offering detailed insights into the most critical and failure-prone regions of the structure under multi-hazard conditions. This level of integration and resolution has not been presented in previous studies, making the proposed methodology a significant contribution to the field of structural and multi-hazard engineering.

As per Figure 1, the framework begins with the hazard model, which estimates intensity measures (IMs) for flood and seismic events. For the seismic hazard, the analysis is based on the conditional mean spectrum (CMS) approach, where the first step involves calculating the uniform hazard curves (UHCs) using probabilistic seismic hazard analysis (PSHA) for a conditioning period (T). In the vulnerability model, advanced CFD simulations were conducted in OpenFOAM (Jasak, 2009) using the Volume of Fluid (VoF) method to model turbulent flow, pressure fluctuations, and

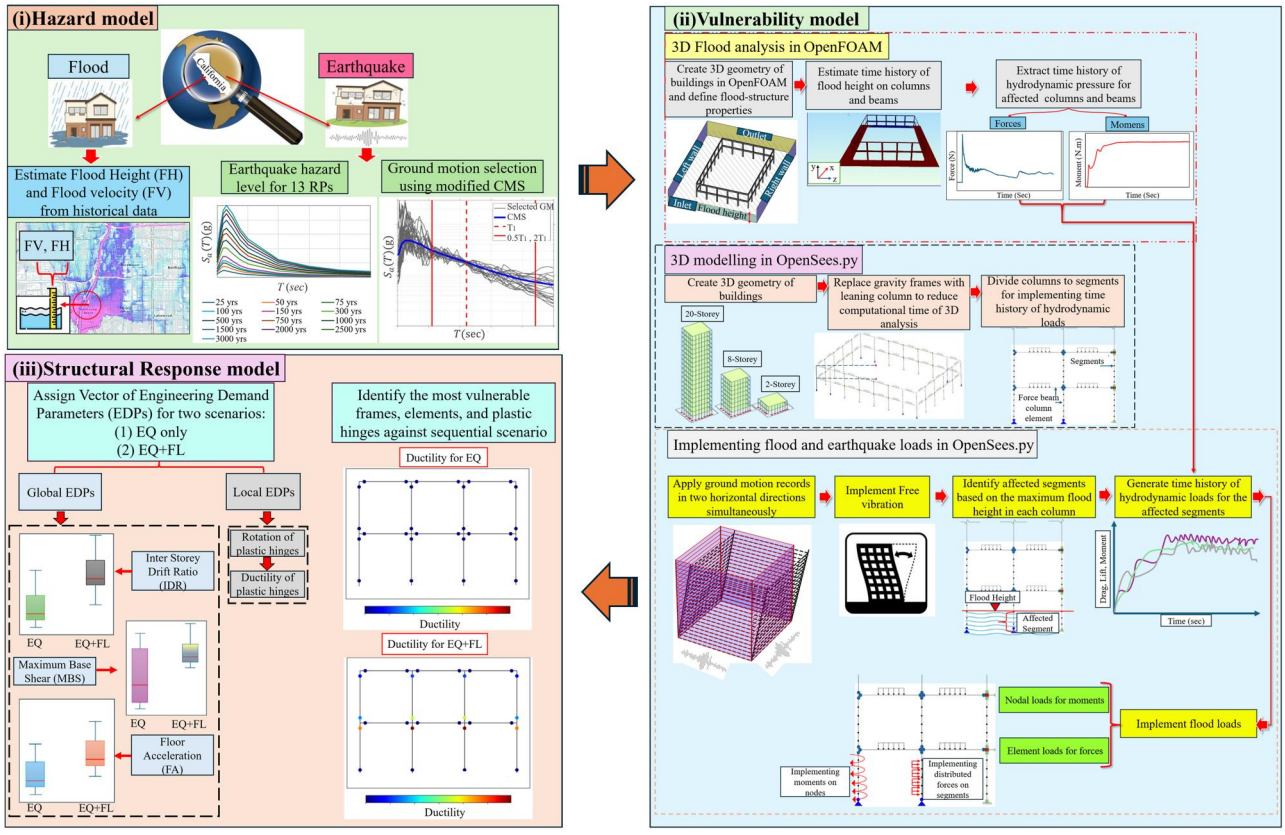

Figure 1. Workflow of the research, including hazard model, vulnerability model, and structural response model.

hydrodynamic forces. These simulations provided detailed data on flood heights, pressures, and forces acting on structural components. The structural response model integrates this CFD data into FE analysis to evaluate structural responses to combined flood and seismic loads, with EDPs identifying the most vulnerable elements. The approach is demonstrated through three case studies of SMRF buildings: low-rise (2-storey), mid-rise (8-storey), and high-rise (20-storey), using 3D nonlinear models to predict building performance during sequential hazards.

3. Case study

3.1. Description of reference buildings

The methodology is applied to low-, mid-, and high-rise SMRF buildings that were originally developed as part of the FEMA P695 (2009) benchmark study. These archetype structures are designed in accordance with ASCE 7-05 (2006) and AISC 341-05 (2005) seismic provisions and are classified under Seismic Design Category D_{max}. All geometric and structural characteristics, including storey heights, bay dimensions, member sections, and material properties, are directly adopted from FEMA P695 and the associated NIST (2010) documentation. These configurations have been widely validated and used in prior studies for collapse fragility and nonlinear dynamic analysis (e.g. Fayaz et al., 2023; Kim & Han, 2021; Torres-Rodas et al., 2021), ensuring consistency with contemporary design practices.

The primary distinction among the 2-storey, 8-storey, and 20-storey frames is building height, which measures 8.40, 31.80, and 78.60 m, respectively. While each building features a first-storey height of 4.5 m, taller than the typical upper-storey height of 3.90 m, this reflects common real-world practice for accommodating commercial spaces, parking, or lobbies at ground level. Crucially, the structural elements in the first storey (particularly the columns) are proportioned with greater stiffness and strength to prevent soft-storey formation. In particular, Torres-Rodas et al. (2021) demonstrated that SMRF buildings exhibit stable and ductile seismic performance without developing soft-storey mechanisms, even when modelled in conjunction with gravity framing systems.

Floors are designed for a live load of 2.38 kN/m^2, a dead load of 4.78 kN/m^2, and a perimeter cladding load of 1.20 kN/m^2. Figure 2 shows the elevation and plan views of these archetypal buildings, each featuring two SMRFs in the X direction and two in the Z direction (marked by dashed red lines) to resist lateral loads. Beam and column dimensions for the three buildings are provided in Tables A.3–A.8 in Supplementary Appendix A, with further details available in NIST (2010), Samadian, Fayaz, Muhit, et al. (2024), and Samadian, Muhit, et al. (2024).

3.2. 3D modelling of the reference buildings

The 3D FE models of the reference buildings were constructed utilising the open-source software OpenSeesPy (Zhu et al., 2018). As illustrated in Figure 2, the structural framework of all SMRFs comprises three-bay frames

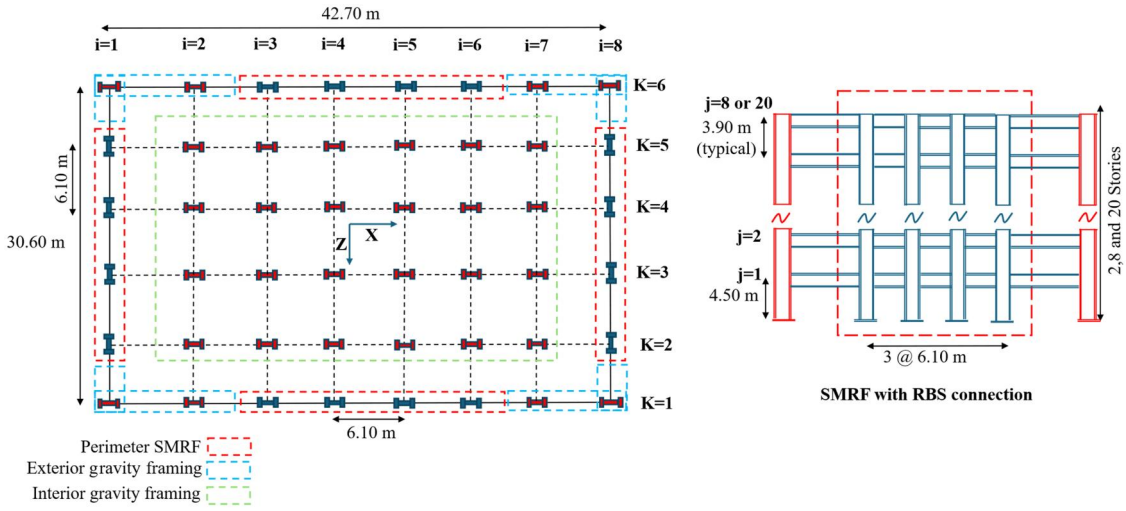

Figure 2. Plan and elevation views of SMRF buildings.

positioned along the building's perimeter in both the X and Z axes. The frames aligned in the X direction are designated from $i=1$ to $i=8$, while those in the Z direction are labelled from $k=1$ to $k=6$. Additionally, each storey level is identified by the variable j. This systematic numbering facilitates the identification of the specific locations of each column and beam, particularly in discussions regarding flood and earthquake analysis outcomes. This research marks the first effort to model the 3D behaviour of SMRF buildings as outlined in NIST (2010). To do so, two 3D models are separately built in OpenSeesPy as follows:

3.2.1. Model with fully gravity frames

Initially, the authors developed a 3D model (referred to as the '*model with fully gravity frames*') that includes the bare structural components of the perimeter SMRFs as well as the interior and exterior gravity framing systems, as illustrated in Figure 2. This model incorporates all relevant aspects of nonlinearity and nonlinear parameters in the perimeter SMRFs. It is noteworthy that in the full 3D model, gravity framing is unable to accommodate the associated P-Δ effects, resulting in the transfer of these effects to the perimeter SMRFs. Exterior and interior gravity frames are interconnected with the perimeter SMRFs in both directions and are modelled using forceBeamColumn elements with pinned connections. In contrast, the beam-column connections of the SMRFs are designed as reduced beam section (RBS) connections, adhering to the guidelines outlined in AISC 341-22 (2022) and AISC 358-22 (2022).

Within the OpenSeesPy, the hinge properties of the RBS are modelled using the Ibarra-Medina-Krawinkler (IMK) bilinear model. Harati and van de Lindt (2024) examined the advantages and disadvantages of fibre and concentrated plasticity methods in the context of tsunami-earthquake scenarios, advocating for the use of concentrated plasticity under multi-hazard conditions. Consequently, beam and column elements are represented as linear elastic, while the hysteretic behaviour of the beam-column connections is modelled using the IMK bilinear model (Ibarra et al., 2005).

Nonlinear rotational springs are incorporated at the ends of the elements, as depicted in Figures 3(b,c), to accurately capture the intended behaviour. A backbone curve is introduced to constrain the modified IK model, as illustrated in Figure 3(c). The properties of this curve are determined by a set of rules that define the hysteretic behaviour and the rate of deterioration. In Figure 3(c), the effective yield strength and rotation are represented by M_y and θ_y, respectively, while the effective stiffness, K_e, is derived from the ratio of M_y to θ_y. For monotonic loading conditions, the capping strength and its corresponding rotation are indicated by M_c and θ_c. The pre-capping and post-capping rotation capacities are denoted as θ_p and θ_{pc}, respectively. Furthermore, the residual strength and ultimate rotation capacity are represented by M_r and θ_u.

This study employs regression equations, calibrated through over 300 experiments on steel-wide flange beams, to ascertain these parameters for various elements, including beams and columns. These equations are informed by the findings of Lignos and Krawinkler (2007, 2011). To familiarise readers with the nonlinear parameters assigned to beams and columns, a comprehensive overview is provided in Supplementary Appendix A, as referenced in Figure 3(c). This includes the equations used to derive the nonlinear hinge properties (Tables A.1 and A.2), as well as the extracted values associated with the modified IK model (Tables A.3–A.8). By providing this level of detail, the study ensures transparency and facilitates reproducibility and verification by other researchers.

In 3D modelling, the nonlinear behaviour of the panel zone was simplified using elastic elements in line with the recommendations of previous studies (Da Silva et al., 2020; Farazmand et al., 2023; Hsiao et al., 2008; Wang et al., 2017; Wieser, 2011), as shown in Figure 3(c). For flood analysis, a critical concern is the risk of shear failure in columns, particularly at lower water levels where increased shear demands may cause failure before reaching the floor level. To address variations in shear capacities of beams and columns under axial loading during earthquake and flood phases, post-processing is essential. Following Harati and

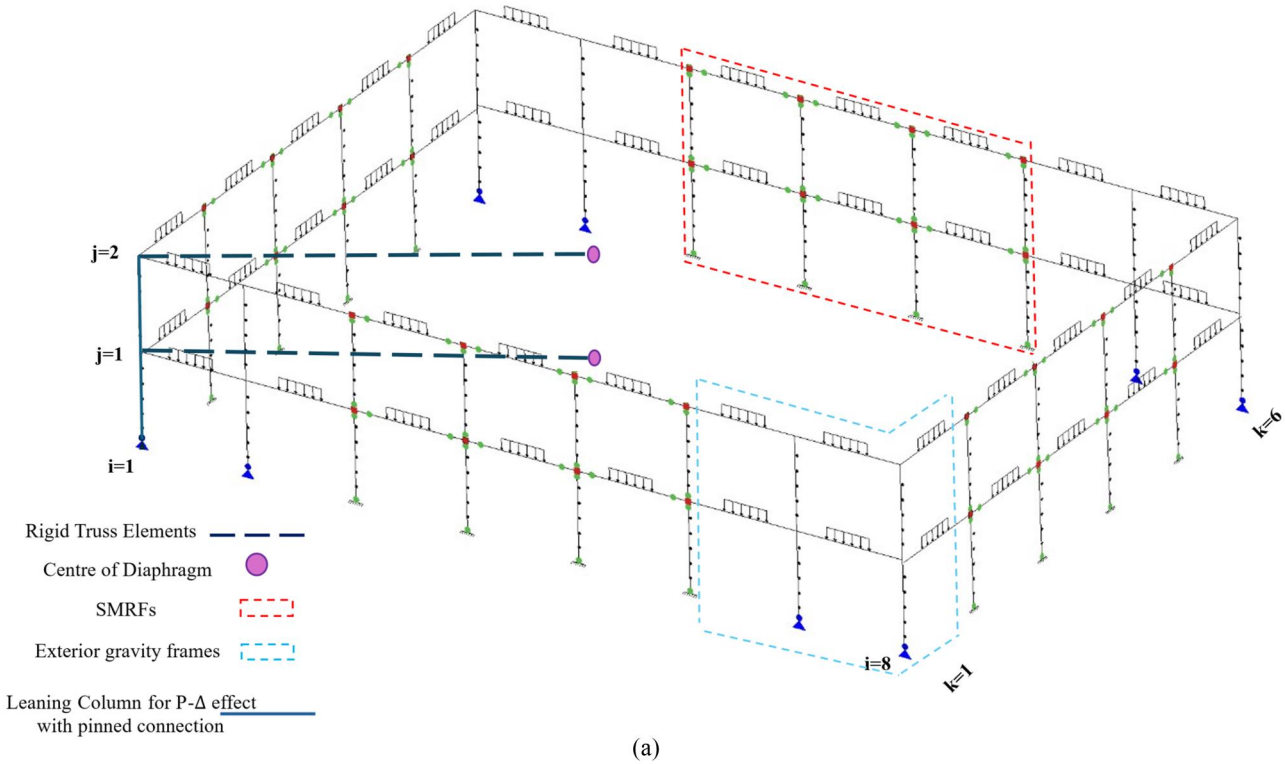

(a)

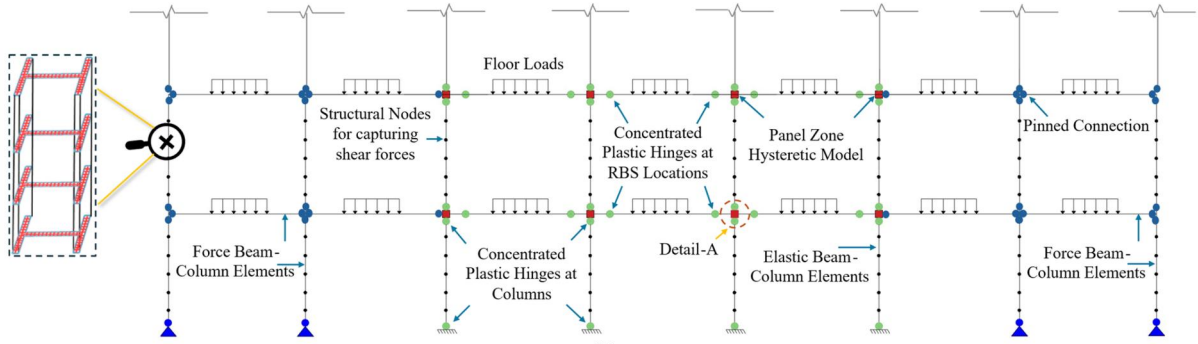

(b)

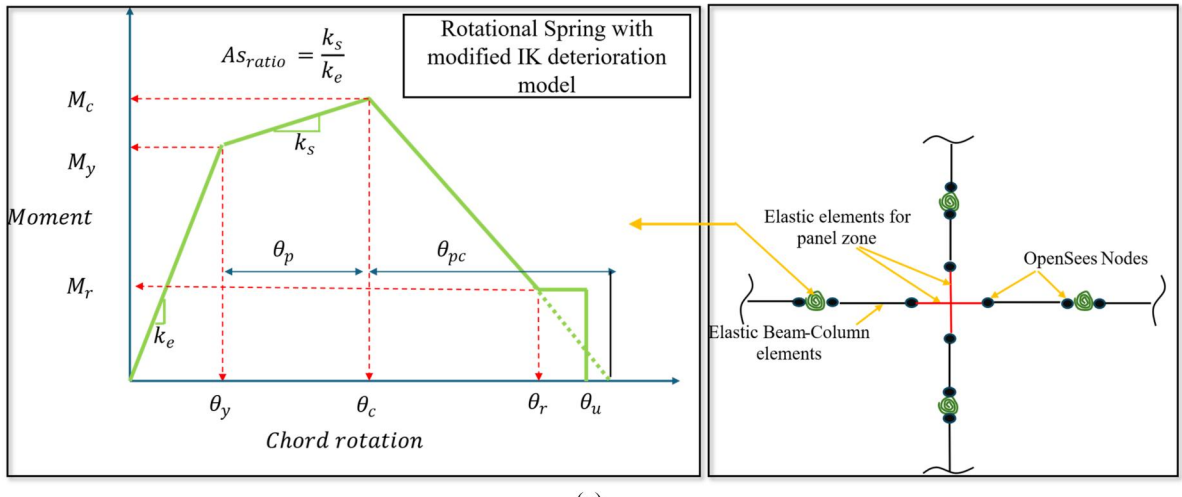

(c)

Figure 3. Details and properties of SMRF buildings: (a) model with leaning column in OpenSeesPy; (b) modelling exterior gravity frames and perimeter SMRFs in OpenSeesPy; (c) detail-A: panel zone modelling and modified IK model.

van de Lindt (2024), post-processing techniques account for shear failure induced by flood-related forces and moments. The results obtained from the post-processing phase are presented and discussed in Section 6.1. Additionally, due to the temporal variation of flood height along the columns, it is crucial to segment the columns into multiple equal-height sections to accurately apply the forces and moments generated by the flood. As illustrated in Figure 3(b), structural nodes are integrated along the columns, and each column is subdivided into smaller segments. Further elaboration on the application of forces and moments to these segments is thoroughly examined in Section 5.2.3.

3.2.2. Model with leaning column

To enhance computational efficiency while preserving the essential nonlinear behaviour of the SMRF system, a modified 3D model, referred to as the 'model with leaning column', was developed. This model retains the same nonlinear stiffness properties of the perimeter SMRFs (see Supplementary Appendix A) but omits the interior gravity frames shown in Figure 2 (green dashed lines). The removal is justified because these gravity columns, with pinned bases and pinned beam-column connections, do not contribute to lateral load resistance and show no nonlinear response under seismic excitation. Additionally, eliminating them significantly reduces computational demand, allowing a sharper focus on the seismic performance of the lateral system.

To account for the P–Δ effects that would normally be carried by the interior gravity frames, a leaning column is introduced. This column, following established practice in 2D nonlinear modelling (Elkady & Lignos, 2015; Lignos et al., 2013; Zareian et al., 2010), is modelled in OpenSeesPy using elastic beam-column elements and connected to the centre of the diaphragm at each storey level *via* axially rigid truss elements with zero rotational stiffness (Figure 3(a)). The leaning column carries the same vertical load as the omitted interior frames, thereby preserving the second-order effects while not adding to lateral stiffness. To verify the reliability of this simplified model, both pushover analysis and NLTHA were conducted for the 2-storey SMRF building. The pushover analysis extended to 6% drift, while NLTHA was performed using four ground motion records representing return periods of 25, 100, 500, and 3000 years, capturing a broad spectrum of seismic intensities from frequent to extreme events. These records were selected from the NGA-West 2 database (Ancheta et al., 2014) and scaled using the modified CMS-based approach proposed by Samadian, Fayaz, et al. (2024), as outlined in Table B.1.

The selection of return periods, 25, 100, 500, and 3000 years, was intended to validate the robustness of the 3D model across a broad spectrum of seismic hazard levels, ranging from frequent, low-intensity events (25 years) and moderate events typical of non-engineered design levels (100 years), to the design basis earthquake (DBE, 500 years) and the maximum considered earthquake (MCE, 3000 years). The comparison between the model with leaning column and the full gravity frame model revealed strong agreement in terms of pushover curves, roof displacement time histories, and maximum inter-storey drift ratios (MIDR), as presented in Figures B.1 and B.2, as well as in Table B.1 in Supplementary Appendix B. Even under the most severe shaking (3000-year return period), both models yielded similar MIDRs of about 4%, demonstrating the robustness of the model with leaning column. Given its accuracy and reduced computational cost, the model with leaning column is adopted throughout the remainder of the paper for multi-hazard analysis. It includes the perimeter SMRFs (red dashed lines in Figures 2 and 3(a)) and all exterior gravity frames (blue dashed lines in Figures 2 and 3(a)), which contribute to lateral stiffness and are retained in the analysis.

To further validate the model, 3D pushover results from OpenSeesPy were compared with 2D pushover curves developed by Samadian, Fayaz, Muhit, et al. (2024) and Samadian, Muhit, et al. (2024) for FEMA P695 archetype frames. The 3D models used lateral load distributions proportional to the first-mode shapes and mass. As shown in Figure B.3, the pushover curves from both studies show close agreement, indicating that the 3D leaning column model accurately reproduces the behaviour of benchmark models. Additionally, the fundamental periods (T_1) calculated from OpenSeesPy for the 2-, 8-, and 20-storey frames are 0.95, 2.48, and 4.53 s, respectively, closely matching the 2D values reported in FEMA P695 (2009), which are 0.91, 2.29, and 4.47 s.

4. Hazard analysis

4.1. Earthquake scenario

To perform NLTHA of the reference buildings under seismic loading, the process begins with a PSHA, followed by ground motion (GM) selection. In this study, rather than using conventional target-spectrum-based selection methods, a modified CMS approach is adopted, as proposed by Samadian, Fayaz, et al. (2024). This method is built upon a prior PSHA conducted for California, from which the UHCs were extracted. These UHCs serve as the foundation for constructing CMS at various hazard levels. The CMS procedure begins by calculating the hazard curve using PSHA for a specified conditioning period (T), which serves as the reference period for defining spectral acceleration demand, $S_a(\mathrm{T})$. The approach further incorporates weighted factors across different time intervals to ensure that selected GMs more accurately reflect the target hazard spectrum at each intensity level. The target IM, $S_a(\mathrm{T})$, is derived from data in the NGA-West 2 database (Ancheta et al., 2014), which includes about 7000 mainshock records from 277 earthquakes. GM selection is done using vector-valued filters with weights tailored to specific structural analysis needs. Samadian's model uses the Index of Agreement (I_A) to assess the similarity between selected GMs and the target spectrum, performing better than previous methods by focusing on the first-mode period, leading to higher EDPs.

The model also accounts for period elongation and higher mode effects. The current study selects GMs for 13 hazard

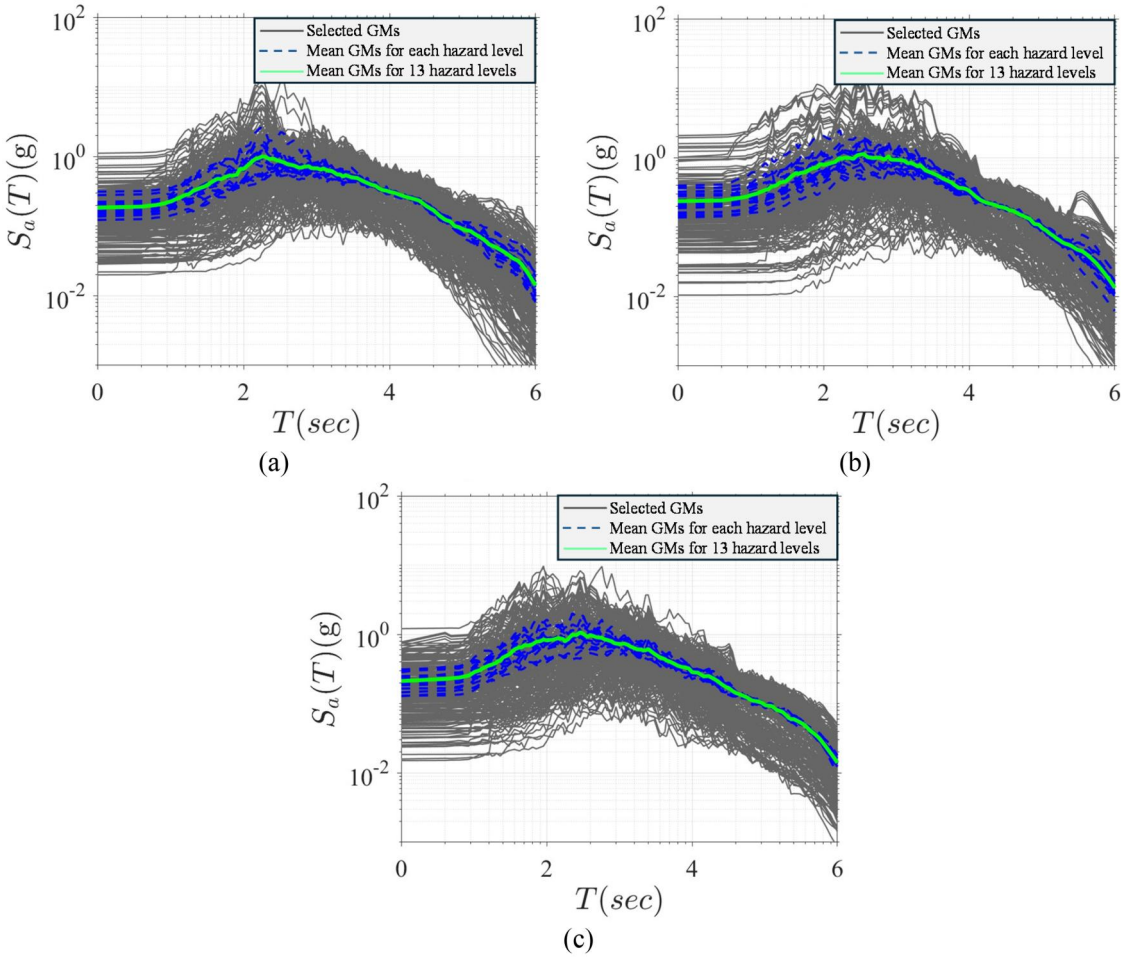

Figure 4. Ground motion selection using modified-CMS for (a) 2-storey; (b) 8-storey; and (c) 20-storey SMRF buildings.

levels (return periods of 25, 50, 75, 100, 150, 300, 500, 750, 1000, 1500, 2000, 2500, and 3000 years), with two horizontal components per record. During scaling, periods are divided into three ranges based on the first-mode period (T_1): (i) S_a(T) at T_1 for the primary mode; (ii) S_a(T) for periods shorter than T_1 ($0.5T_1$ to T_1) capturing higher modes; (iii) S_a(T) for periods longer than T_1 (T_1 to $2T_1$) capturing nonlinear behaviour and period elongation. Weighting factors are applied to each range, with higher weights recommended for periods exceeding T_1 in low-rise structures, and for periods shorter than T_1 in mid- and high-rise buildings. This method is used for 2-, 8-, and 20-storey buildings, selecting 20 GM records per hazard level and direction, totalling 520 GM records per building. The selected records and the mean spectrum are shown in Figure 4.

4.2. Flood scenario

This study investigates building responses to combined seismic and flood hazards by analysing four flood depths, 0.30, 1, 2, and 4 m, chosen to represent a spectrum from moderate to severe flooding. These levels are informed by Sanders et al. (2022), whose high-resolution flood hazard maps of the Greater Los Angeles Basin revealed significant underestimations in federal flood assessments, such as FEMA's. Their work indicates that flood depths exceeding 0.30 m pose serious risks, threatening 197,000–874,000 residents and $36–$108 billion in assets. They emphasise 30 cm as a critical safety threshold for both structures and occupants. The hazard curve used centres on 100-year flood events, highlighting the potential for flood depths over 1.7 m in Los Angeles due to atmospheric rivers and spring snowmelt, both amplified by climate change (Sanders et al., 2022; UCIrvine News, 2022).

In the Los Angeles region, fluvial and pluvial floods are the primary sources of risk, with shallow floods (3–10 cm) typically from local runoff and deeper events (>100 cm) linked to river overflows and insufficient drainage systems (Sanders et al., 2022). Sanders et al. (2022) identified a high-risk corridor between South Gate and Long Beach along the Los Angeles and San Gabriel Rivers. Urbanisation has amplified runoff, while ageing infrastructure, such as channels, drains, and dams, struggles to manage increasing flood volumes (LACDPW, 2024; USACE, 2011, 2016, 2022). Reports from the US Army Corps of Engineers and Los Angeles County Public Works show many river segments are undersized or degraded due to sedimentation, vegetation growth, and damage (USACE, 2011, 2016, 2022). Furthermore, flood risk assessments for California classify several dams as 'urgent' or 'urgent and compelling' for repairs, indicating significant infrastructure vulnerabilities (Sanders et al., 2022).

Jones (2019) supports calls for re-evaluating California's flood intensity models. Sanders et al. (2022) further reinforce that flood depths beyond 0.30 m substantially impair structural safety, supporting this study's use of 0.30, 1, 2, and 4 m flood heights to simulate increasingly severe scenarios (Sanders et al., 2022; UCIrvine News, 2022). These conditions are particularly relevant as climate change is expected to intensify atmospheric river events, making deep, widespread flooding more frequent. For each specified flood height (FH), the corresponding flood velocity (V) is calculated as follows (FEMA, 2014):

$$V = 0.3048.(105.6 \times FH)^{0.50} \quad (1)$$

4.3. Interaction of two hazards

Although the probability of floods and earthquakes occurring simultaneously is low, sequential events, such as a flood following or preceding an earthquake, are common in regions like California that are prone to both hazards (Ge et al., 2023; Wang et al., 2014). The literature identifies three categories of hazard interaction, as outlined by Argyroudis et al. (2019): (i) uncorrelated hazards of different types, such as independent floods and earthquakes occurring at different times; (ii) correlated or cascading hazards, where one hazard triggers another, examples include liquefaction, landslides, or tsunamis initiated by earthquakes, or floods and debris flows following hurricanes; and (iii) repeated or similar hazard types (e.g. mainshocks and aftershocks) that impose cumulative structural impacts over time. For sequential earthquake-flood scenarios, several studies are on bridges (Banerjee & Prasad, 2013; Dong et al., 2013; Guo et al., 2016; Prasad & Banerjee, 2013) and masonry schools (Vatteri et al., 2022), often treating the hazards as independent. Some research (Korswagen et al., 2019) suggests that while earthquake intensity can influence the likelihood of subsequent flooding (e.g. *via* levee failure), the flood's magnitude typically remains independent of the earthquake's intensity. In such cases, the failure of levees, whose integrity is described by vulnerability curves based on empirical data, acts as the connecting mechanism between the two hazards.

In line with similar multi-hazard studies for California (Banerjee & Prasad, 2013; Wang et al., 2014), the current investigation assumes that flooding is independent of seismic activity. Potential flood sources include: (i) failure of ageing infrastructure such as river channels, drainage systems, and dams (LACDPW, 2024; USACE, 2011, 2016, 2022); and (ii) extreme precipitation events driven by climate change, particularly atmospheric rivers, which can result in large-scale flooding (Sanders et al., 2022; UCIrvine News, 2022). While seismic activity can lead to infrastructure failure, it is not the sole cause of flood risk in Southern California. As noted by UCIrvine News (2022), climate-induced precipitation extremes are a significant standalone threat. Accordingly, this study adopts a two-step approach: first, assessing the impacts of the initial hazard (earthquake) on the structure, and then evaluating the effects of the second hazard (flood) on the same structure, which has already been damaged or altered by the first hazard. Although flood-first scenarios are also of interest and could yield valuable insights, this study prioritises the more commonly adopted earthquake-first sequence for buildings, which aligns with prior research (Harati & van de Lindt, 2024; Korswagen et al., 2019; Xu et al., 2021) and enables the assessment of flood fragility in already damaged structures.

5. Vulnerability analysis

5.1. Numerical modelling approach for flood simulation

Flood loads on structures such as buildings, bridges, and coastal infrastructure have traditionally been assessed using simplified methods like the Equivalent Lateral Load (ELL) and Variable Depth Pushover (VDPO) approaches (Attary et al., 2021; FEMA P-259, 2012; Kelman, 2022; Petrone et al., 2020; Tagle et al., 2021). These methods apply force distributions based on assumed water depths and are suitable for early design stages. However, they fall short in capturing the spatial and temporal variability of hydrodynamic forces, particularly under turbulent or wave-influenced conditions. Static approaches like ELL and VDPO do not consider critical flow phenomena such as turbulence, separation, or pressure differentials around complex geometries, often resulting in inaccurate force estimations during extreme flood events such as wave overtopping or rapid inundation.

To address these limitations, this study uses OpenFOAM, an open-source CFD tool that allows for full 3D simulation of fluid-structure interaction. OpenFOAM captures forces along all three axes (X, Y, and Z) and the associated moments about these axes, enabling accurate assessment of both translational and rotational effects induced by asymmetric or transient flow patterns. This high-resolution modelling captures detailed flow behaviours, such as eddies and splashes, that static methods overlook, making it a powerful tool for evaluating structural vulnerability. Previous studies (Le et al., 2024; Pregnolato et al., 2022; Winter et al., 2018) confirm that CFD-based analysis in OpenFOAM provides more realistic predictions of flood-induced forces and structural response, thus supporting safer and more resilient design practices.

5.1.1. Set up computational domain and geometry of the buildings

The simulation geometry is constructed using ANSYS (2024), with results subsequently exported to OpenFOAM. The spatial relationship between the floodwaters and the building can significantly affect the velocity due to various hydrodynamic phenomena, including flow obstruction, turbulence, stagnation zones, and wake formation. In this investigation, the flood velocity, calculated using Equation (1), is established at the reservoir location within the numerical domain utilised in OpenFOAM, following a dam-break simulation scenario. This scenario presupposes a sudden failure of the dam, which permits the floodwaters to flow downstream under the influence of gravity (Motley et al., 2016). To ensure that the velocity and height of the floodwaters, as estimated by Equation (1), were consistent between the reservoir and the building site, a sensitivity

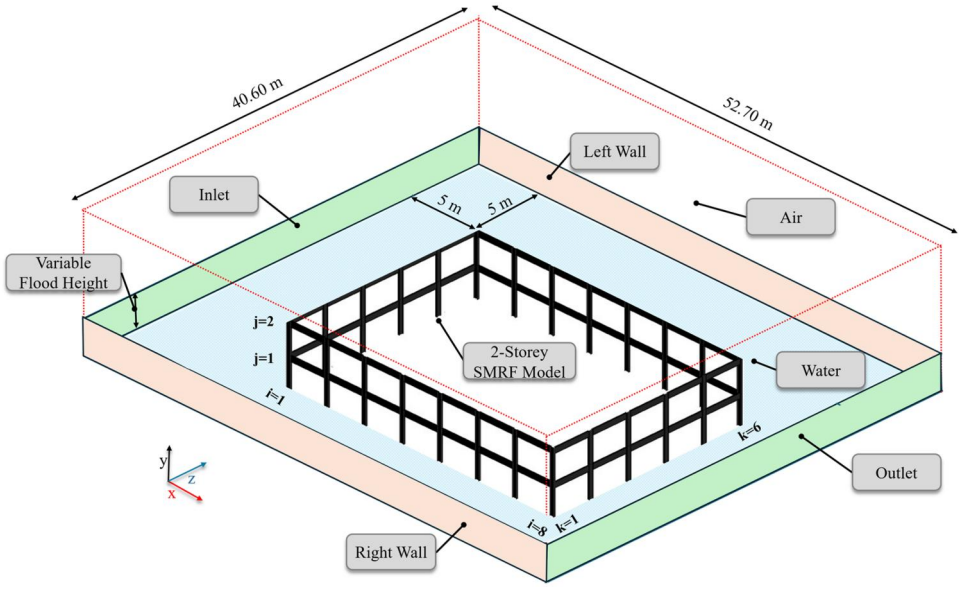

Figure 5. Schematic representation of the domain defined in OpenFOAM for the 2-storey SMRF building.

analysis was carried out to determine an appropriate inlet-to-building distance. Four different distances, including 2, 5, 10, and 20 m, were considered.

For each configuration, the hydrodynamic forces acting on a representative front-facing column were evaluated to assess how the inlet position affects flow development and resulting loads. The analysis revealed that when the inlet was placed too close to the building (e.g. 2 m), the flow did not have sufficient space to develop before reaching the structure, leading to unrealistic force estimations. At moderate distances (5 and 10 m), the flow reached a more stable and realistic profile, resulting in consistent and representative hydrodynamic loading on the structure. Increasing the distance beyond this (e.g. 20 m) had no appreciable effect on the magnitude of the forces, indicating that the flow had already stabilised before interacting with the structure. Based on these findings, a 5-m inlet distance was selected as the optimal configuration, as it provides a reliable representation of the flood behaviour while maintaining computational efficiency. Consequently, as illustrated in Figure 5 and Figure B.4(a), the computational domain is configured to be 52.70 m in length, 40.60 m in width, and 8.40 m in height, with a 5-m separation maintained between the reservoir and each side of the building. Additionally, OpenFOAM necessitates a minimum water volume behind the reservoir to initiate the simulation; therefore, this study considers a minimum water width of 1 m for various flood height levels, as depicted in Figure B.4(a).

5.1.2. Turbulence modelling

In the context of this flood simulation, turbulence is addressed through the Reynolds-Averaged Stress (RAS) methodology, which streamlines the Reynolds-Averaged Navier-Stokes (RANS) equations by averaging the stress components. The standard k-ε turbulence model is specifically utilised, which characterises turbulence by resolving two primary variables: turbulent kinetic energy (k) and the turbulent dissipation rate (ε). The governing RAS equations are derived from the averaged momentum and continuity equations under the assumption of incompressible flow. The Reynolds stress terms are represented using the Boussinesq approximation, which establishes a relationship between the Reynolds stresses and the velocity gradients. The equations pertinent to turbulence modelling are:

$$\begin{aligned} \frac{\partial k}{\partial t} + \nabla.(kU) &= P_k - \varepsilon \\ \frac{\partial \varepsilon}{\partial t} + \nabla.(\varepsilon U) &= C_{\varepsilon 1}\frac{\varepsilon}{k}P_k - C_{\varepsilon 2}\frac{\varepsilon^2}{k} \end{aligned} \tag{2}$$

where P_k is the production of turbulent kinetic energy, $C_{\varepsilon 1} = 1.44$, $C_{\varepsilon 2} = 1.92$, and $C_\mu = 0.09$ are standard model constants. The turbulent viscosity, ϑ_t is calculated as:

$$\vartheta_t = C_\mu \frac{k^2}{\varepsilon} \tag{3}$$

This methodology effectively captures the primary influences of turbulence while avoiding the need to resolve the complete spectrum of turbulent fluctuations, thereby enhancing computational efficiency for extensive simulations such as flood modelling.

5.1.3. Multiphase flow and VoF methodology

The interFoam solver is employed to simulate the interaction between the two phases of water and air throughout the flooding event. This solver utilises the VoF technique to monitor the interface between these two incompressible fluids. An indicator function, α_1, is implemented to represent the presence of each fluid within the domain, with a value of 1.0 denoting regions occupied by water and a value of 0.0 indicating the presence of air. Values in between signify cells that are part of the free interface. This approach guarantees a well-defined interface between air and water, which is essential for accurately representing the wave fronts and interactions that occur during flooding. The governing VoF

equation for the transport of the phase indicator is:

$$\frac{\partial \alpha_1}{\partial t} + \nabla.(\alpha_1 U) = 0 \tag{4}$$

where U is the shared velocity field of the two fluids. The Navier-Stokes equations are applied across the entire domain, incorporating the effects of surface tension and gravitational forces that influence fluid interactions at the interface. The simulation utilises standard fluid characteristics for air and water, specified as follows: densities: $\rho_{air} = 1\,\text{kg/m}^3$; $\rho_{water} = 1000\,\text{kg/m}^3$; kinematic viscosities: $\vartheta_{air} = 1.48(10^{-5})\,\text{m}^2/\text{s}$, $\vartheta_{water} = 1.0(10^{-6})\,\text{m}^2/\text{s}$; surface tension: $\sigma = 0.07\,\text{N/m}$. These properties are critical in determining the momentum transfer and interactions between the air and water phases throughout the flood simulation.

5.1.4. Boundary and initial conditions

The boundary and initial conditions are established for all significant variables: (i) phase indicator (α_1): Initialised to represent the initial distributions of water and air, where $\alpha_1 = 1$ indicates water and $\alpha_1 = 0$ indicates air; (ii) velocity (U): A no-slip condition (fixedValue) is enforced at solid boundaries, ensuring fluid adherence to surfaces such as the ground or structures. At open boundaries, a zero-gradient condition is implemented; (iii) pressure (p): A zero-gradient condition is applied at outlet boundaries, permitting dynamic pressure adjustments based on the flow field. At the upper boundary, a fixed total pressure is set to simulate atmospheric conditions. (iv) turbulence quantities (k and ε): Wall functions are utilised for solid boundaries to account for turbulence effects near the wall, while zero-gradient conditions are applied at outlet boundaries.

5.1.5. Meshing and temporal discretisation

The meshing is created using ANSYS, ensuring accurate representation of design features and high-quality mesh, especially in critical areas like the water-air interface and near solid boundaries with steep flow gradients. The meshing process employs the *MultiZone* method with the following configurations: the Mapped Mesh Type is designated as *Hexa*, while the Free Mesh type is configured as *Hexa Core*. The Surface Mesh Method is controlled by the program, the Element Order is specified as *Linear*, and the Element size is established at 0.25 m. Figure B.4(b) shows a detailed view of the geometry and meshing developed for the 2-storey SMRF building. Mesh resolution is enhanced in areas of high significance, such as near structural components and other regions of interest within the fluid domain, to effectively capture vital flow characteristics and ensure numerical precision. Subsequently, the mesh is exported from ANSYS and imported into the OpenFOAM environment for simulation purposes. The simulation employs adaptive time-stepping in accordance with the Courant-Friedrichs-Lewy (CFL) condition, maintaining a maximum Courant number of 0.5. This approach ensures numerical stability by constraining the time step size in relation to local flow velocities and cell dimensions:

$$\Delta t \leq \frac{C_{\max} \Delta x}{|U|} \tag{5}$$

5.1.6. Solver configuration

The simulation uses OpenFOAM's interFoam solver, which employs the PIMPLE algorithm, combining the PISO and SIMPLE methods, for efficient pressure-velocity coupling in transient multiphase flows. This solver handles incompressible, immiscible fluid dynamics by computing a unified velocity field and pressure for both phases, with phase fraction equations representing the interface. Flow rates at various velocities and depths are applied at the inlet boundary using the variableHeightFlowrate condition. To simulate free-surface flooding interactions with structures, interFoam incorporates the VoF method for interface tracking and the k-ω SST turbulence model to capture turbulent flow. Table B.2 details the boundary conditions used, while Figure 5 shows the boundary conditions and domain configuration for the two-storey SMRF building.

5.2. CFD results

The CFD model developed in OpenFOAM was first validated to ensure the accuracy and reliability of the 3D simulation. Following successful validation, the CFD results are presented in this study. Supplementary Appendix C provides the details of the validation process and sensitivity analysis. Due to page limitations, figures are shown only for the 2-storey SMRF building as a representative case in this section, while results for the 8-storey and 20-storey buildings, though not illustrated, are still discussed in the manuscript. The methodology and findings are applicable across all cases, as the primary difference lies in the height of the SMRF buildings, and the investigation approach remains consistent, ensuring that the results and conclusions can be comprehended and extrapolated without redundancy. Water height is recorded on each column and beam to identify structural elements impacted by flood waves, with only these elements subjected to flood loads. Structural components are labelled using a system where each label consists of one letter followed by three digits: the first digit represents the storey level (j), the second denotes the i-location, and the third indicates the k-location (e.g. C111 refers to a column on the first storey at $i = 1$, $k = 1$, as per Figures 2 and 5).

Figure 6 displays the OpenFOAM simulations and fluid patterns on beams and columns at various intervals for different flood heights (FH). Figure B.5 illustrates the water profile and its temporal variations on the affected columns for four different FH in the 2-storey building, where for the FH = 4 m, all outer beams and columns on the first storey (C111–C116, B112–B116) and the second storey (C211–C216, B212–B216) facing the flood are impacted within 3 s. Columns on the right side (C111, C121, C131, etc.) and symmetrical left-side elements experience similar patterns, with only first-storey beams affected. At FH = 2 m, all front columns across both stories and the first-storey beams are impacted. Side columns on the first storey and specific beams on the right (B111–B141) and left sides (B136–

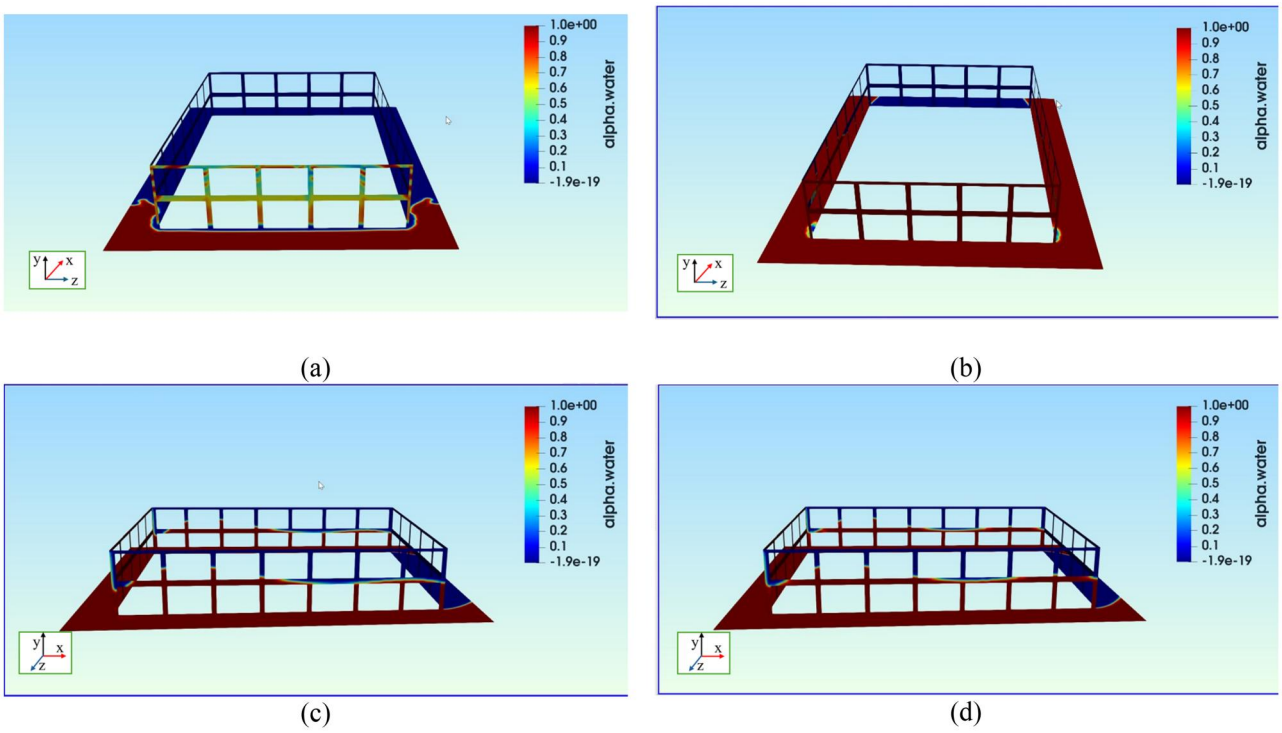

Figure 6. OpenFOAM simulation for the 2-storey SMRF building with FH = 4 m at: (a) 1 s; (b) 5 s; (c) 10 s; (d) 20 s.

B166) are also affected. For FH = 1 m, only the first-storey front columns (C111–C116) and eight side columns are inundated, while no beams sustain damage. At FH = 0.30 m, only six front columns (C111–C116) are affected. All elements at the domain's outlet remain unaffected across flood scenarios, highlighting specific vulnerabilities based on flood height.

5.2.1. Description of drag, lift, and moment

This section examines the hydrodynamic forces, drag, lift, and moment affecting beams and columns that are fully or partially submerged during flood loading. The drag force (F_x) acts in the direction of water flow along the X-axis, while lift forces act perpendicular to this direction: F_y for front-facing columns and F_z for side columns. Overturning moments (primarily M_y) develop due to the asymmetric distribution of these forces. Significant moments arise around the vertical (Y) axis, driven by drag-induced torsion and unequal pressure between upstream and downstream elements. The dominance of M_y over M_x and M_z indicates that most rotational deformation occurs about the vertical axis, consistent with the direction and nature of flood forces. While M_x (rotation about the flow axis) is minimal due to the direct alignment with the flood path, and M_z (side-to-side rotation) remains small due to relatively balanced vertical lift, M_y captures the critical torsional behaviour induced by floodwaters.

5.2.2. Hydrodynamic forces and moments on beams and columns

Figure 7 shows fluid load outputs from OpenFOAM for columns and beams affected by flooding at an inundation level of FH = 4 m. Columns on the upstream side experience the greatest forces due to direct flood engagement, with drag forces peaking at 750,000 N for lower columns (C112–C115) initially, then stabilising around 250,000 N. Higher-level columns (C211–C216) experience reduced drag. Lift forces on the front columns, ranging from 750 to 2000 N initially, decrease as the flood progresses, stabilising around 100–250 N. Upper-storey columns experience higher lift forces due to flow dynamics influenced by the first-storey columns and structural components. The front columns experience significant moment forces, reaching up to 8,000,000 N.m, resulting in torsional and bending stresses, particularly at lower levels. Moment forces stabilise but remain significant for lower-level columns.

The moment distribution is symmetric for columns on both sides of the flood flow, including the second-storey level. Figures 7(d–i) shows that columns on the right side of the flood experience minimal drag compared to lift forces. Columns closer to the advancing flood experience higher forces, with drag forces positive and lift forces negative on the right side, due to pressure differences. Notably, the first column in the flood path (C111) records lower values of F_x, F_z, and M_y compared to subsequent columns (C121, C131), due to flow separation and vortex shedding. This causes a low-pressure area behind C111, leading to higher forces on C121, which is in the wake of C111. Vortex shedding around columns C111 and C116 is also shown in Figure 6(b).

Columns like C121 and C131 initially experience drag forces up to 700 N, which stabilise as the flood progresses, while columns farther from the inlet encounter lower drag forces (~250 N). Lift forces are most significant on lower-level columns like C121 and C131 during the initial flood impact, with higher-level columns experiencing reduced forces due to increased distance from the flood

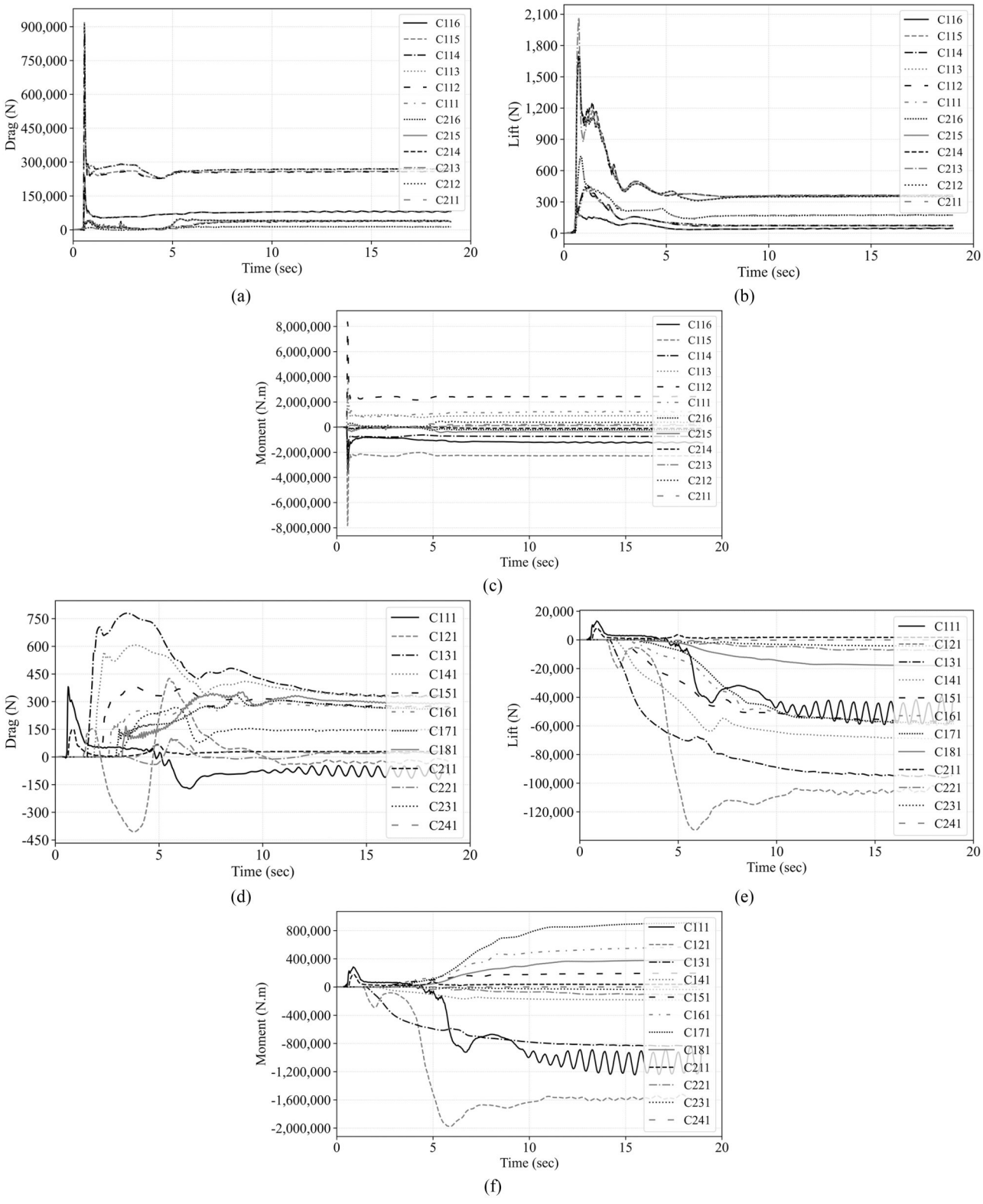

Figure 7. Time history of hydrodynamic loads on columns for the 2-storey SMRF building with FH = 4 m: (a–c) hydrodynamic loads for front columns; (d–f) hydrodynamic loads for columns on the right-hand side of the flow.

base. As shown in Figure 7(f), moment forces on the right-side columns peak early in the flood, with C121 reaching up to 2,000,000 N.m. The combination of drag and lift forces generates torsional and bending stresses, with moments often influenced by recirculating flow, leading to negative values for certain columns, indicating twisting forces. A similar pattern is observed for the left-side columns; however, their corresponding figures are omitted for brevity.

The analysis of beam interactions with floodwaters (Figures 8(a–c)) shows that front-facing beams experience the highest drag forces, particularly lower-level beams (B112–B116), which peak at 750,000 N within the first 1–2 s. As floodwaters progress, these forces stabilise at lower levels,

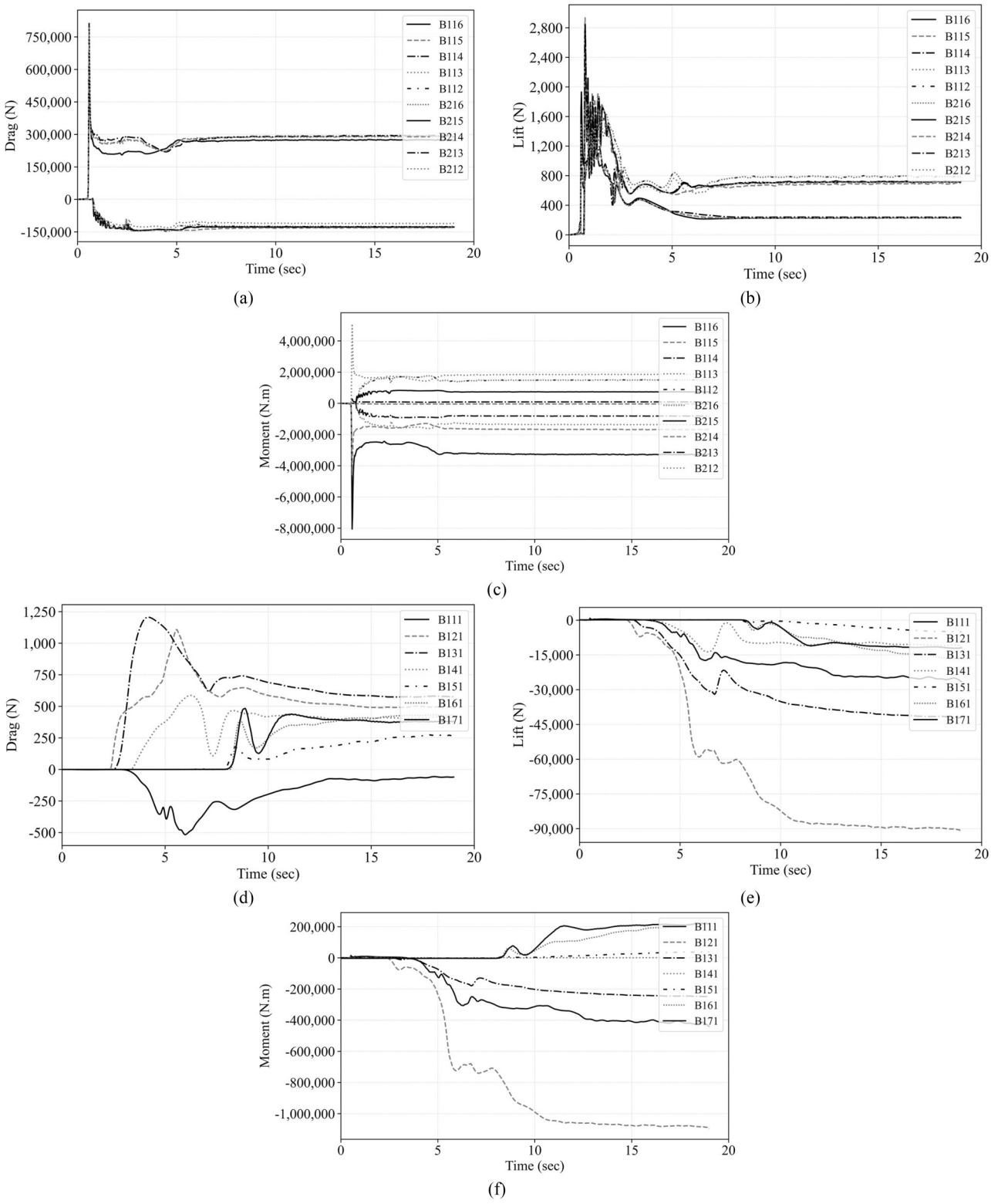

Figure 8. Time history of hydrodynamic loads on beams for the 2-storey SMRF building with FH = 4 m: (a–c) hydrodynamic loads for front beams; (d–f) hydrodynamic loads for columns on the right-hand side of the flow.

while higher-level beams (B212–B216) encounter reduced drag. Flow separation can occur, with positive drag forces on first-storey beams and negative drag forces (suction effect) on second-storey beams due to recirculating flow. Lift forces on front-facing beams, peaking between 2000 and 3000 N for lower-level beams, decrease after the initial impact but remain higher for upper-level beams.

Figure 8(c) depicts the moment forces on front-facing beams, illustrating significant torsional and bending stresses from drag and lift forces. Beams on both sides of the structure, especially on the first storey, are impacted the most (Figures 8(d–f)). Right-side beams experience peak drag forces of 1200 N for B131, and moment forces reach nearly 1,100,000 N.m during the initial impact. Lower-level beams

and columns face the greatest forces, especially at the onset of flooding, with recirculation and turbulent flow intensifying these effects. Torsional and bending stresses, particularly at lower elevations, must be accounted for in design. Flood analysis indicates that the second column on both sides of the flood flow endures the highest hydrodynamic forces due to vortex shedding, making it particularly vulnerable. Hydrodynamic loads for the 2-storey SMRF building at inundation levels of 2, 1, and 0.30 m are shown in Figures B.6–B.9 in Supplementary Appendix B.

For the 8-storey building, beams on the right-hand side experience significant hydrodynamic effects under a 4 m flood depth. During the initial flow surge, drag forces on lower and mid-storey beams peak between 400 and 500 N, while upper-storey beams exhibit milder responses. Lift forces are consistently negative, with uplift forces exceeding −150,000 N on mid-storey beams, particularly between 10 and 20 s. Moment demands vary by storey, with both positive and negative peaks reaching approximately ±1,000,000 N·m, highlighting the complexity of flow–structure interactions. Front-facing beams also experience substantial hydrodynamic loads during flooding. Drag forces increase over time, peaking around 400 N for several lower- and mid-height beams. Lift forces rise sharply, exceeding 1000 N in some lower-storey beams around 2 s into the analysis, indicating strong upward buoyancy effects. Moment demands vary more widely, with some beams reaching positive moment peaks over 2,500,000 N·m and negative peaks up to −5,000,000 N·m, further emphasising the dynamic and nonlinear nature of the structural response. Overall, the magnitude of forces is strongly elevation-dependent, with lower-level beams subjected to the highest demands.

For the right-hand side columns, drag forces increase rapidly after 3 s, peaking between 400–450 N for several members before stabilising. Lift forces remain predominantly negative, dropping below −150,000 N, indicating substantial upward hydrodynamic pressure. Moments fluctuate significantly, with peaks exceeding ±2,000,000 N·m, reflecting strong overturning effects particularly at the lower levels. Front-facing columns show a progressive increase in drag force during the flood event, with peak values reaching around 300,000 N, especially for mid-height columns such as C112, C113, C114, and C115. Lift forces peak around 750 N in the early stages of the analysis, then diminish and stabilise near zero. Moment demands increase notably, reaching up to 4,000,000 N·m in first-storey columns like C115 and C111. These results indicate that the first-storey front-facing columns are subjected to the most intense hydrodynamic forces due to their direct exposure to rising and flowing floodwaters.

For the 20-storey building, the flood profile and time history closely resemble those of the 8-storey building. This is because the maximum considered flood depth of 4 m does not reach above the eighth storey. In both cases, the flood flows across the front-facing columns and beams, rising to a certain height before stabilising below the upper threshold. Since the flood intensity remains consistent between the two buildings, the distribution and evolution of hydrodynamic forces follow a similar pattern, particularly for structural elements within the inundated zone.

The results reveal several structural behaviours under flood loading that would be overlooked using simplified or static load assumptions. One significant observation is the presence of dominant out-of-plane moments, My, resulting from asymmetrical water impact and vortex shedding. These torsional effects induce twisting in structural elements, especially corner and side columns, that are typically neglected in conventional ELL methods. The hydrodynamic moment demand, especially at lower stories, exceeds initial expectations and interacts with previously damaged plastic hinges, compounding localised stress concentrations. Additionally, wake effects and flow separation behind leading-edge columns (e.g. C111) result in unexpected pressure amplifications on downstream elements (e.g. C121), as seen in Figure 7. These patterns highlight the importance of full 3D CFD modelling in capturing secondary and spatially heterogeneous forces. Such phenomena have direct implications for design codes, as they suggest current simplified flood loading prescriptions may significantly underestimate critical demands in multi-hazard-prone areas.

5.2.3. Implementing effects of earthquake and flood in OpenSeesPy

The proposed methodology is designed to explicitly capture accumulated structural damage and progressive deterioration using a sequential NLTHA approach. This process is achieved through the following two key mechanisms:

i. **Damage accumulation in the concentrated plastic hinges**
   The numerical model in this study adopts a concentrated plastic hinge approach, specifically utilising the modified IK deterioration model, which accounts for: yield strength deterioration; post-capping strength deterioration; and unloading stiffness deterioration. When the earthquake event occurs, the structure undergoes nonlinear deformations, and the plastic hinges form and accumulate damage. Unlike elastic models, damage is not reset when the flood loading starts; instead, the weakened structure with existing residual deformations and reduced stiffness continues to experience further loading. This ensures that the flood impact is applied to a structure that has already been damaged by the earthquake, rather than an undamaged or idealised model. This damage persistence is a fundamental feature of the modified IK model and ensures that the multi-hazard interaction is realistically captured.
ii. **Sequential loading approach: earthquake followed by flood**
   The sequential analysis procedure includes the following steps.

Step (1) Earthquake Loading Phase: The building is subjected to nonlinear seismic loading, where the structural response to seismic ground motion is analysed across 13

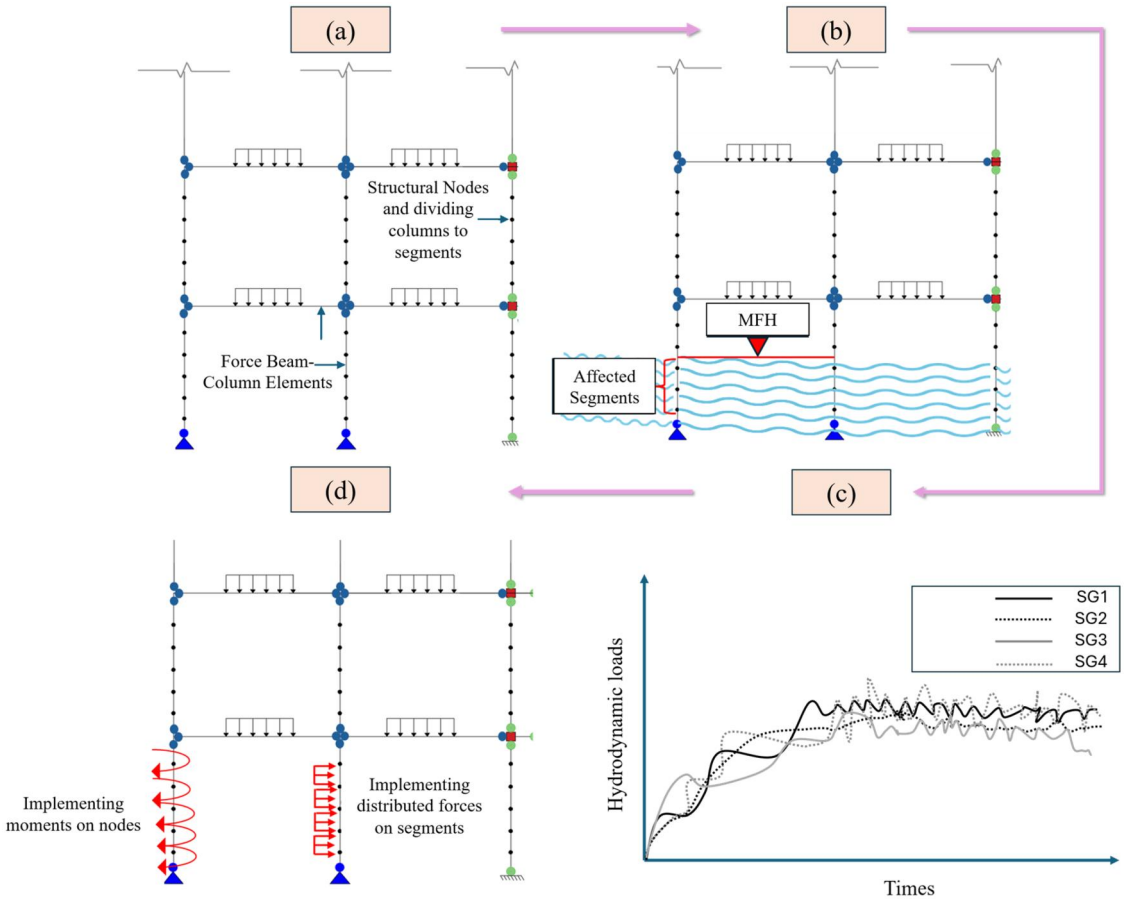

Figure 9. Implementing flood loads on columns in OpenSeesPy.

hazard levels, each incorporating 20 ground motion records applied simultaneously in two horizontal directions. For each analysis corresponding to varying seismic intensities, key EDPs such as inter-storey drift ratio (IDR), floor acceleration (FA), and maximum base shear (MBS) are extracted as global EDPs. Additionally, the rotation of plastic hinges in beams and columns is computed as local EDPs in response to the earthquake loading. If the building reaches the collapse drift ratio, the analysis is terminated, as structural failure is assumed to have occurred. If the building survives the earthquake (i.e. does not reach collapse drift ratio), the analysis proceeds to the flood-loading phase.

Step (2) Flood Loading on a Damaged Structure: The post-earthquake damaged building is then subjected to hydrodynamic flood loads extracted from OpenFOAM simulation, commencing after a free vibration analysis is conducted between successive evaluations. The flood loads are applied while retaining all damage states from the earthquake, meaning that the structure continues to deteriorate under additional hydrodynamic pressures. To facilitate the application of hydrodynamic loads, a Python module has been developed that effectively implements these loads on columns and beams. To do so, the following steps are defined:

i. Each column is divided into multiple segments (SG) of uniform height (SGH), with each section operating as an independent column, as illustrated in Figure 9, Step (a).
ii. The maximum flood height (MFH) for each column is derived from the floodwater time history (Figure 9, Step (b)).
iii. Utilising the MFH obtained from OpenFOAM, the number of segments potentially impacted by the flood (SG_{po_aff}) is identified (Figure 9, Step (b)). For instance, as per Figure 9, Step (b), four segments of the first storey columns are affected by a given flood level.
iv. At each time step, it is necessary to assess whether the flood affects each SG_{po_aff} based on its SGH. If an SG_{po_aff} is impacted by the flood at that specific time, the corresponding hydrodynamic force and moment values are extracted from the flood history of the column for that SG_{po_aff}. Conversely, if the SG_{po_aff} is not affected, the force and moment values for that time will be recorded as zero.
v. The flood load time history for each column is allocated across the SG_{po_aff}, resulting in each SG_{po_aff} possessing its own distinct time history of flood hydrodynamic pressure (Figure 9, Step (c)). Following the establishment of the flood load time history for each segment, the subsequent phase involves the application of forces and moments to each SG_{po_aff}. As depicted in Figure 9, Step (d), forces are applied at the elemental

level in OpenSeesPy, while moments are applied using a nodal load object. To apply moments at the nodes, the tributary area of each SG_{po_aff} is first determined. The moment for each SG_{po_aff} is then allocated between its upper and lower nodes in accordance with the tributary area. Similarly, for the beams, those that are influenced by the flood are identified first, and then the flood's time history is applied to the beams based on the tributary area associated with each beam.

Step (3) Recording Structural Response: Two distinct EDPs are reported: At the end of the earthquake event (reflecting purely seismic damage); At the end of the flood event (reflecting the combined effects of earthquake and flood loading). This allows for a direct comparison of how flood loading exacerbates seismic damage, providing insights into multi-hazard vulnerability.

6. Structural response model

6.1. Global EDPs

After completing the NLTHA for 13 seismic hazard levels and four FHs for each building, a vector of global EDPs is derived, including IDR, FA, and MBS. Figure 10 presents boxplots of global EDPs for the two-storey SMRF building across four flood levels with two scenarios: (i) Earthquake (EQ) and (ii) Earthquake combined with Flood (EQ + FL). The short bars indicate the minimum and maximum values, while the inner lines represent the 25th, 50th, and 75th percentiles. As per Figure 10(a), the median IDR for the two-storey building under EQ is uniform across the height and complies with code limits, with storey drift values ranging from 0.25 to 1%, below FEMA P-58's 1% threshold (FEMA P58-1, 2012) and consistent with previous SMRF research (Guan, 2021). Also, the mean floor accelerations are in line with previous studies (Samadian, Muhit, et al., 2024).

However, as shown in Figures 10(a,b), integrating flood loads with earthquake forces leads to significant variations in IDR and FA, with disparities increasing as flood levels rise. For instance, at a 4-m flood level, IDR of the first storey under EQ + FL is nearly eight times higher than under EQ alone (Figure 10(a)), highlighting the impact of flood loads. At flood levels of 2, 1, and 0.30 m, the IDR for the first storey remains relatively unchanged, with values of 0.0224, 0.0098, and 0.0095, respectively, while the second storey remains at 0.0044. For the EQ-only scenario (Figure 10(b)), the median FA for the first floor is 0.19, and 0.22 g for the second floor, consistent with earlier SMRF seismic studies (Samadian, Muhit, et al., 2024). In the EQ + FL scenario, the first floor's median FA rises significantly to 0.41, 0.32, 0.31, and 0.29 g at 4, 2, 1, and 0.30-m FHs, respectively, while for the second floor, it rises to 0.77, 0.44, 0.32, and 0.31 g. Finally, Figure 10(c) shows that flood levels of 4 and 2 m cause a greater increase in the median MBS than lower flood levels (1 and 0.30 m).

In the post-processing phase, the shear capacity of each column segment (V_c) was computed using the expression $V_c = 0.6 \times F_y \times A_w$, where A_w is the effective shear area of the web, calculated as $A_w = (d - 2t_f) \times t_w$. Here, d denotes the section depth, t_f is the flange thickness, and t_w represents the web thickness. From the sequential earthquake and flood analyses, the maximum shear force experienced by each segment was extracted and compared against this computed shear capacity. If the shear demand exceeded the corresponding capacity, the affected column segment was deemed to have failed in shear. For the 2-storey SMRF building, a total of 1983 instances of column shear failure were recorded at a flood height of 4 m. The most severely affected were Column C166 on the left-hand side and Columns C121 and C151 at the front face of the structure. These failures are likely attributed to torsional effects caused by flood-induced asymmetry, combined with the high exposure at the leading edge of the flood flow. Additional shear failures were observed in Columns C112, C117, C128, C148, and C158 on the first storey, as well as C215 and C265 on the second storey.

When the flood height was reduced to 2 m, the number of shear failure instances dropped significantly to 160. At this level, Columns C121 and C151, again located at the front face of the first storey, remained the most affected. No shear failures were recorded in the second-storey columns under this flood condition. A similar pattern was observed for a flood height of 1 m, with the number and distribution of failures closely resembling those at 2 m. For a flood height of 0.3 m, no shear failures were detected in any of the columns.

6.2. Local EDPs

This study also examines the performance of plastic hinges under sequential EQ and EQ + FL scenarios using OpenSeesPy, considering them as local EDPs. The maximum plastic hinge rotation (θ_{max}) for each column and beam was extracted, normalised by the yielding rotation (θ_y), and used to estimate ductility (μ). Figures 11–14 show median ductility values for different frame configurations of a two-storey building under EQ and EQ + FL scenarios with hazard return periods of 25 and 3000 years. Frames $k = 1$ and $k = 6$ are aligned with the X direction, and frames $i = 1$ and $i = 8$ with the Z direction. Under the 25-year EQ scenario (Figure 11), the plastic hinges of the beams in the first storey and in the first and third bays of both Frames $i = 1$ and $i = 8$ exhibit the highest ductility. In contrast, for Frames $k = 1$ and $k = 6$, the beams in the second storey and the first and third bays demonstrate the greatest ductility. Notably, the ductility for all beams remains below 1, indicating that all plastic hinges operate within the elastic range without yielding. However, for the 3000-year EQ scenario (Figure 12), beam hinges show inelastic ductility, with the highest ductility in second-storey beams for Frames $k = 1$ and $k = 6$, and first-storey beams for Frames $i = 1$ and $i = 8$.

Figures 11(c,d) illustrate that the columns of Frames $i = 1$ and $i = 8$ demonstrate greater rotation and ductility than those in $k = 1$ and $k = 6$, albeit still within elastic limits, with the top hinges of the inner columns at the first storey showing greater

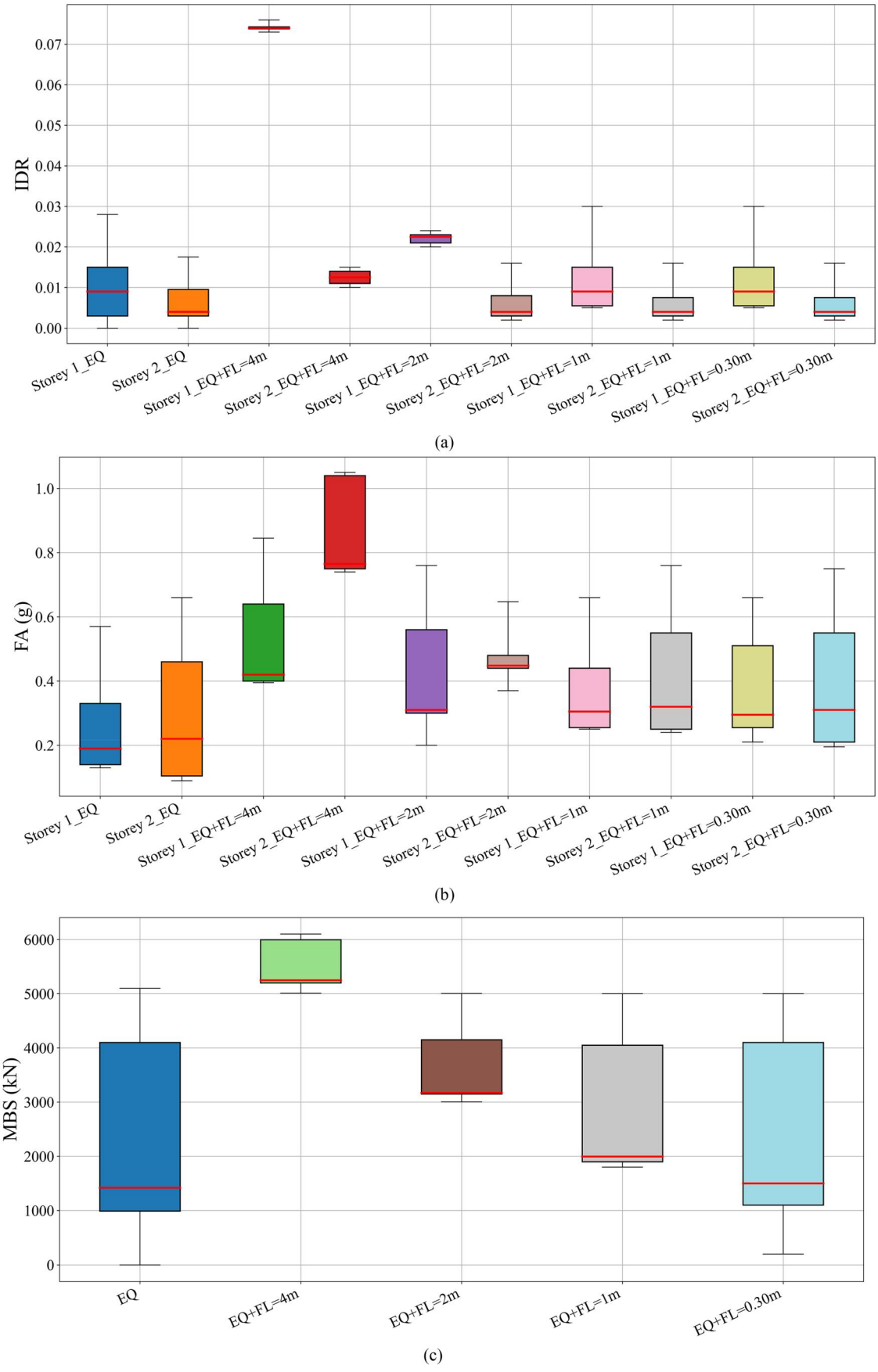

Figure 10. Global EDP values for the 2-storey SMRF building: (a) IDR; (b) FA; (c) MBS.

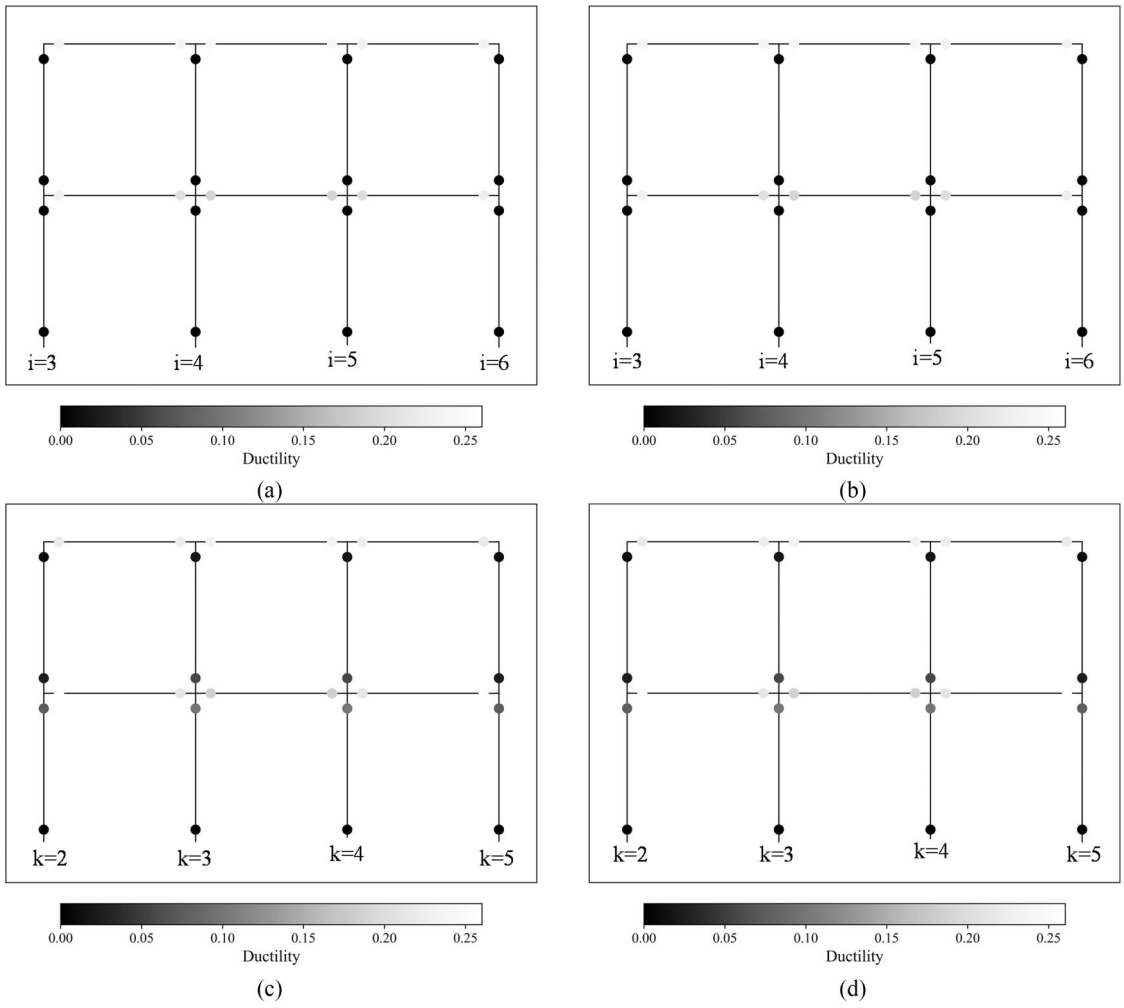

Figure 11. Plastic hinge ductility for beams and columns under EQ scenario for the hazard level of 25 years for frames: (a) $k = 1$, (b) $k = 6$, (c) $i = 1$, and (d) $i = 8$.

ductility than those of the outer columns at the same level. The two-storey SMRF has pinned base connections, with bottom hinges of first-storey columns showing zero rotation, while all other column hinges exceed the elastic range during the 3000-year EQ scenario. When EQ is combined with flooding, plastic hinges in both beams and columns experience a substantial increase in ductility. For example, under a 25-year EQ with a 4-m flood (Figure 13), all plastic hinges in beams and columns of Frames $i = 1$ and $i = 8$ yield and undergo significant rotation due to intense hydrodynamic pressures. The inner columns, particularly at the first-storey top and second-storey bottom, experience the greatest ductility.

As shown in Figures 7(a–c), columns C112-C115, which are heavily affected by flooding, show the highest drag and moment values, leading to the greatest ductility in their plastic hinges. The flood load causes asymmetric forces, resulting in greater rotation in the front columns ($\mu = 150$) compared to the back columns ($\mu = 110$), which are indirectly affected by the sequential hazard. Although the back columns are not directly impacted by the flood, the sequential multi-hazard effect implies that the earthquake has already compromised the overall structural integrity. Consequently, this effect may lead to a redistribution of flood forces throughout the structure, causing the back columns to endure some degree of indirect loading as the building deforms under the flood pressure exerted on the front. Nevertheless, the intensity of the hydrodynamic forces acting on the back columns remains lower than that on the front columns. Therefore, while the back columns do experience some increase in rotation, their rotation remains less than that of the front columns. For the 3000-year EQ with a 4-m flood (Figure 14), ductility increases further in the inner columns of Frames $i = 1$ and $i = 8$, reaching 170 and 140, respectively.

7. Discussion on the limitations of results

It is important to acknowledge that the results of this research are subject to specific assumptions and limitations. The findings are based on the particular structural configuration analysed in this study, which corresponds to selected earthquake and flood intensity measures. While the SMRF considered here is a widely used steel frame typology globally, applying the methodology to other structural systems would require following the framework outlined in Figure 1. One key limitation is the assumption of a fixed-base condition, which excludes the effects of SSI. Although this simplification is common in multi-hazard analysis, future research should expand the framework to incorporate SSI, particularly for soft-soil sites where foundation flexibility may

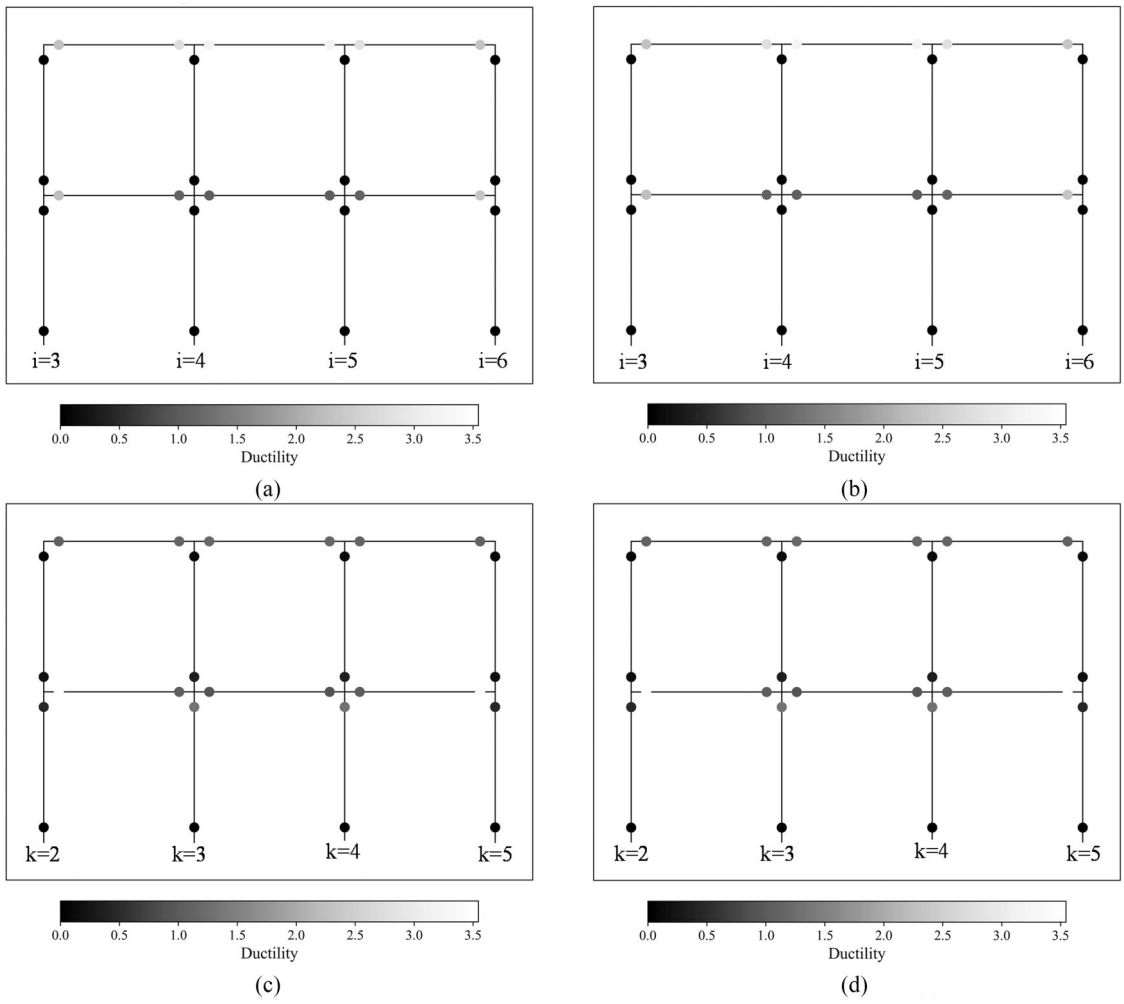

Figure 12. Plastic hinge ductility for beams and columns under EQ scenario for the hazard level of 3000 years for frames: (a) $k = 1$, (b) $k = 6$, (c) $i = 1$, and (d) $i = 8$.

significantly influence the structural response under sequential earthquake and flood loading.

Another key point relates to the integration of probabilistic analysis within the framework. A fully probabilistic treatment was not implemented for the CFD simulations or NLTHA due to their computational demands. Instead, the probabilistic component was incorporated through the seismic hazard analysis and flood scenario selection. For seismic loading, a comprehensive PSHA was conducted using the modified CMS approach, accounting for 13 return periods ranging from 25 to 3000 years. This enabled the selection of ground motions that are statistically representative of varying intensity levels and consistent with de-aggregated site-specific hazard characteristics. For flood loading, four representative flood depths, 0.30, 1, 2, and 4 m, were selected to span a range of realistic hazard scenarios from common to extreme events. Thus, while the CFD simulations themselves were deterministic, they were repeated across multiple flood intensities to approximate a range of possible flood demands. These choices reflect a semi-probabilistic approach that balances methodological rigour with computational feasibility.

This study also focuses on capturing the nonlinear behaviour of primary structural components, particularly beams and columns, under sequential multi-hazard loading. Non-structural components such as infill walls were not considered in the current analysis. This exclusion was based on the assumption that, under strong earthquake excitation, infill walls experience early-stage damage or failure, reducing their influence on subsequent flood response. Nonetheless, incorporating non-structural components in future extensions of this framework would offer a more comprehensive understanding of building vulnerability and could be accomplished by implementing discrete infill wall models in OpenSeesPy.

8. Conclusions

This research established and implemented a comprehensive framework for evaluating the performance of steel special moment-resisting frame (SMRF) buildings of varying heights, low, mid, and high, when exposed to multiple hazard scenarios, particularly earthquakes (EQ) and floods (FL). The extreme floods analysed here are not earthquake-driven; instead, they represent high-intensity flood events that could occur independently in Los Angeles (LA), particularly due to climate-related factors. However, the multi-hazard framework developed in this study remains applicable for future

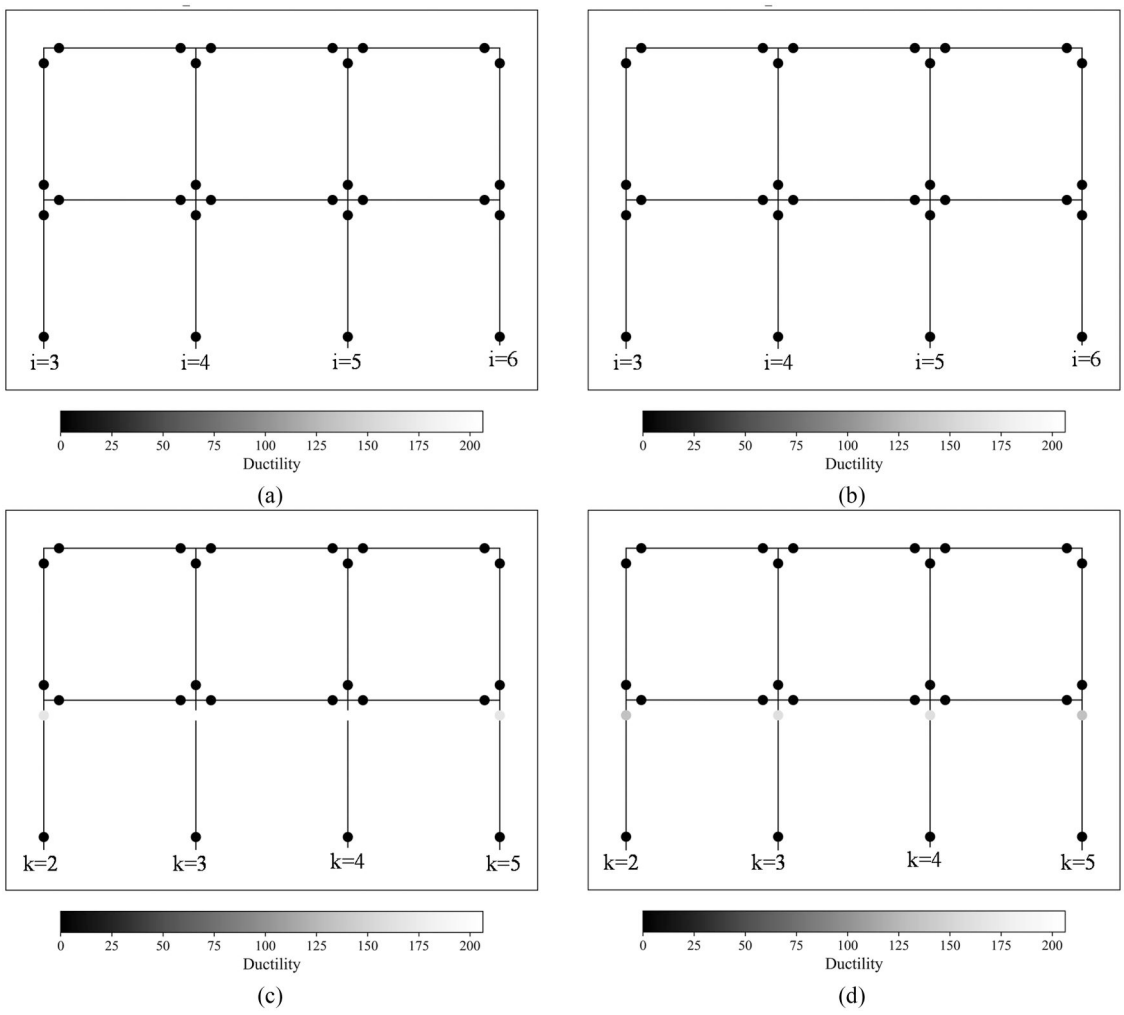

Figure 13. Plastic hinge ductility for beams and columns under EQ + FL scenario for the hazard level of 25 years for frames: (a) $k = 1$, (b) $k = 6$, (c) $i = 1$, and (d) $i = 8$.

extensions, including correlated earthquake-flood scenarios, if needed. Rather than relying on traditional two-dimensional (2D) computational fluid dynamics (CFD) or Equivalent Lateral Load (ELL) methods, a three-dimensional (3D) time history analysis was conducted using OpenFOAM. The hydrodynamic forces were subsequently extracted and transferred to OpenSeesPy to facilitate a 3D nonlinear time history analysis (NLTHA) for the sequential EQ + FL scenarios.

Results highlight complex structural behaviours under time-varying flow, including vortex shedding, turbulence, wake effects, and flow separation around structural elements like columns. Also, the FL + EQ scenario can significantly intensify structural responses compared to earthquake-only scenarios. For example, for the two-storey SMRF building, the inter-storey drift ratio (IDR) during a seismic event remains below FEMA P-58's 1% demolition threshold, but in EQ + FL scenarios, the first-storey IDR escalates from 0.0065 (EQ only) to 0.0739 with a 4-m flood height. The second-storey IDR increases to 0.0125 at the highest flood level, indicating that FL + EQ loads at high inundation levels push structures beyond elastic limits. Moreover, floor acceleration (FA) increases significantly under combined hazards: FA in the second storey rises from 0.24 g (EQ only) to 0.83 g (EQ + FL with 4-m height). Similarly, maximum base shear (MBS) values rise due to hydrodynamic pressures from flooding. In the EQ + FL scenario, plastic hinges in the beams and columns of the first storey show significant yielding, especially in frames facing the flood flow, where hydrodynamic forces are strongest. The dominant out-of-plane hydrodynamic loads highlight the need for 3D modelling over 2D in EQ + FL scenarios. The research emphasises the need to re-evaluate structures in flood-prone and earthquake-prone areas and incorporate multi-hazard design principles.

While the case studies presented in this paper focus on SMRF buildings, the integrated framework is designed to be modular and extensible. The sequential coupling of CFD-derived flood forces with nonlinear time-history earthquake simulations is not limited to SMRF structures or steel materials. The methodology can be adapted to other structural systems, including reinforced concrete (RC) or masonry, by substituting appropriate hysteretic models and geometry-specific loading paths. Furthermore, although the present study models an earthquake-first sequence, the workflow can be modified to accommodate reverse sequences (flood-

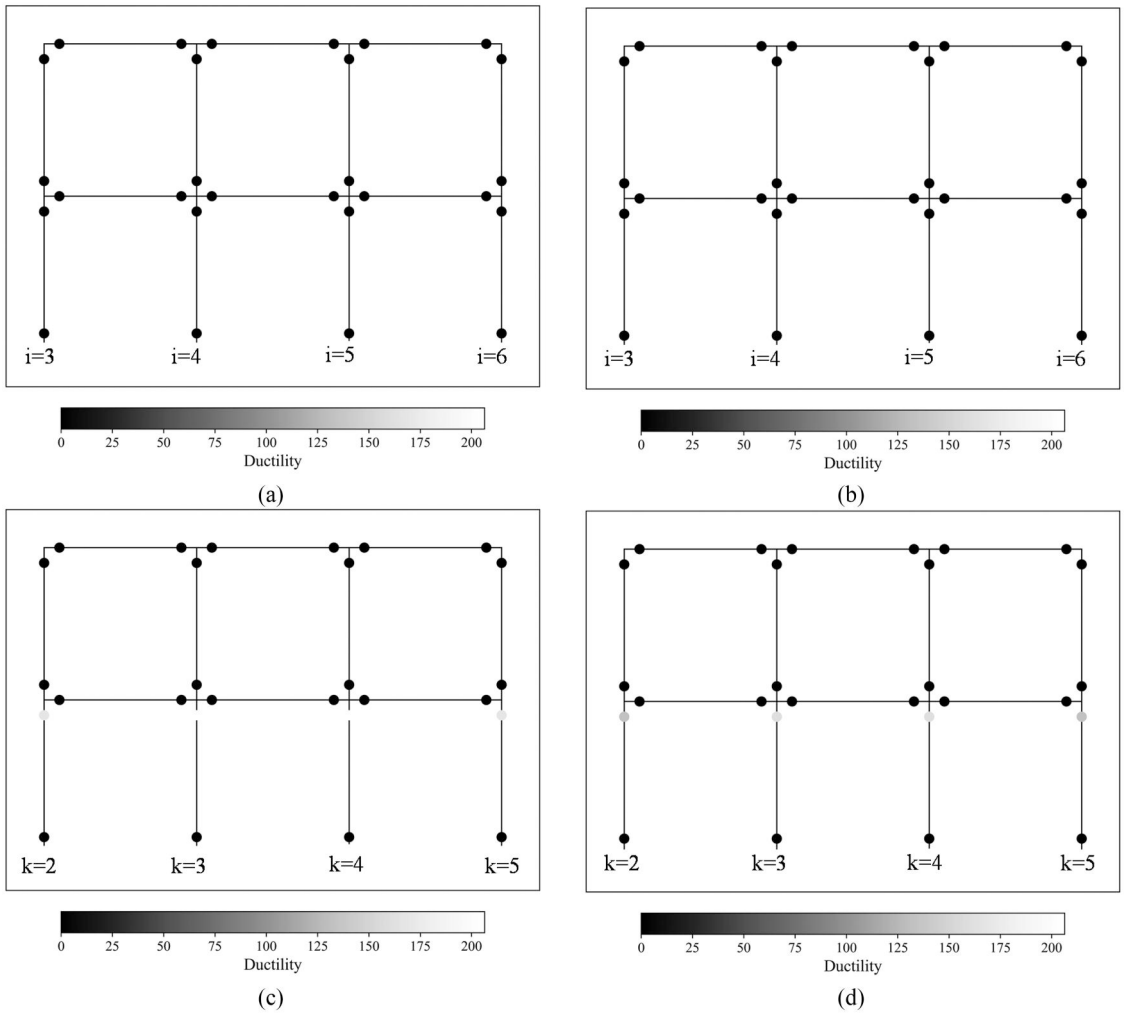

Figure 14. Plastic hinge ductility for beams and columns under EQ + FL scenario for the hazard level of 3000 years for frames: (a) $k = 1$, (b) $k = 6$, (c) $i = 1$, and (d) $i = 8$.

first-then-earthquake), cascading hazards, or even simultaneous interactions, scenarios that are increasingly relevant under climate-driven compound hazard conditions. Similarly, the fluid-structure interaction model can be adapted for coastal flooding or tsunamis with minimal modification. Therefore, the framework provides a foundational basis for broader multi-hazard risk assessments in both research and applied engineering contexts.

Author contributions

CRediT: **Delbaz Samadian**: Conceptualization, Formal analysis, Investigation, Methodology, Software, Validation, Visualization, Writing – original draft; **Hadi Eslamnia**: Software, Validation, Writing – review & editing; **Imrose B. Muhit**: Conceptualization, Investigation, Methodology, Project administration, Supervision, Writing – review & editing; **Maria Pregnolato**: Conceptualization, Methodology, Writing – review & editing; **Nashwan Dawood**: Conceptualization, Project administration, Writing – review & editing.

Disclosure statement

No potential conflict of interest was reported by the author(s).

References

American Institute of Steel Construction (AISC 341-05). (2005). *Seismic provisions for structural steel buildings*. American Institute of Steel Construction (AISC). ANSI/AISC.

American Institute of Steel Construction (AISC 341-22). (2022). *Seismic provisions for structural steel buildings*. American Institute of Steel Construction (AISC). ANSI/AISC.

American Institute of Steel Construction (AISC 358-22). (2022). *Prequalified connections for special and intermediate steel moment frames for seismic applications*. American Institute of Steel Construction (AISC). ANSI/AISC.

American Society of Civil Engineers (ASCE 7-05). (2006). *Minimum design loads and associated criteria for buildings and other structures*. Reston, Virginia: American Society of Civil Engineers, ASCE/SEI 7–05.

Ancheta, T. D., Darragh, R. B., Stewart, J. P., Seyhan, E., Silva, W. J., Chiou, B. S.-J., Wooddell, K. E., Graves, R. W., Kottke, A. R., Boore, D. M., Kishida, T., & Donahue, J. L. (2014). NGA-West2 database. *Earthquake Spectra*, *30*(3), 989–1005. https://doi.org/10.1193/070913EQS197M

ANSYS (2024). Retrieved April 10, 2024, from https://www.ansys.com/en-gb

Argyroudis, S. A., & Mitoulis, S. A. (2021). Vulnerability of bridges to individual and multiple hazards–floods and earthquakes. *Reliability Engineering & System Safety*, *210*, 107564. https://doi.org/10.1016/j.ress.2021.107564

Argyroudis, S. A., Mitoulis, S. A., Winter, M. G., & Kaynia, A. M. (2019). Fragility of transport assets exposed to multiple hazards:

State-of-the-art review toward infrastructural resilience. *Reliability Engineering & System Safety*, *191*, 106567. https://doi.org/10.1016/j.ress.2019.106567

Asad, M., Thamboo, J., Zahra, T., & Thambiratnam, D. P. (2024). Out of-plane failure analysis of masonry walls subjected to hydrostatic and hydrodynamic loads induced by flash floods. *Engineering Structures*, *298*, 117041. https://doi.org/10.1016/j.engstruct.2023.117041

Attary, N., Van De Lindt, J. W., Barbosa, A. R., Cox, D. T., & Unnikrishnan, V. U. (2021). Performance-based tsunami engineering for risk assessment of structures subjected to multi-hazards: Tsunami following earthquake. *Journal of Earthquake Engineering*, *25*(10), 2065–2084. https://doi.org/10.1080/13632469.2019.1616335

Banerjee, S., & Prasad, G. G. (2013). Seismic risk assessment of reinforced concrete bridges in flood-prone regions. *Structure and Infrastructure Engineering*, *9*(9), 952–968. https://doi.org/10.1080/15732479.2011.649292

Daniell, J., & Armand, V. (2012). *The CATDAT Damaging Earthquakes Database 2011—The year in review: CEDIM Research Report 2012-01*. Center for Disaster Management and Risk Reduction Technology (CEDIM). https://www.researchgate.net/publication/258434309_The_CATDAT_Damaging_Earthquakes_Database_2011_-_The_Year_in_Review_CEDIM_Research_Report_2012-01/citations

Da Silva, L. S., Oliveira, S., Costa, R., & Gentili, F. (2020). Design and analysis of steel structures considering the 3d behaviour of the joints. *Advanced Steel Construction*, *16*(2), 137–145. https://doi.org/10.18057/IJASC.2020.16.2.5

Dong, Y., & Frangopol, D. M. (2017). Probabilistic life-cycle cost-benefit analysis of portfolios of buildings under flood hazard. *Engineering Structures*, *142*, 290–299. https://doi.org/10.1016/j.engstruct.2017.03.063

Dong, Y., Frangopol, D. M., & Saydam, D. (2013). Time-variant sustainability assessment of seismically vulnerable bridges subjected to multiple hazards. *Earthquake Engineering & Structural Dynamics*, *42*(10), 1451–1467. https://doi.org/10.1002/eqe.2281

Dong, Z.-Q., Li, G., Song, B., Lu, G.-H., & Li, H.-N. (2022). Failure risk assessment method of masonry structures under earthquakes and flood scouring. *Mechanics of Advanced Materials and Structures*, *29*(21), 3055–3066. https://doi.org/10.1080/15376494.2021.1884322

Elkady, A., & Lignos, D. G. (2015). Effect of gravity framing on the overstrength and collapse capacity of steel frame buildings with perimeter special moment frames. *Earthquake Engineering & Structural Dynamics*, *44*(8), 1289–1307. https://doi.org/10.1002/eqe.2519

EM-DAT (2024). *Global damage costs from natural disasters*. EM-DAT, CRED/UCLouvain, "Natural disasters" [original data]. Retrieved May 13, 2025, from https://ourworldindata.org/grapher/damage-costs-from-natural-disasters

Fairuz, G., Marthanty, D. R., & Sjah, J. (2020). Evaluation of building structure resilience due to flood disaster that are outside the riverbanks in the floodplains. *Applied Mechanics and Materials*, *897*, 239–244. https://doi.org/10.4028/www.scientific.net/AMM.897.239

Farazmand, M., Behnamfar, F., & Aziminejad, A. (2023). Effects of the vertical and horizontal components of near-field ground motions on the seismic behavior of buildings considering soil-structure interaction. https://doi.org/10.21203/rs.3.rs-3626087/v1

Fayaz, J., Torres-Rodas, P., Medalla, M., & Naeim, F. (2023). Assessment of ground motion amplitude scaling using interpretable Gaussian process regression: Application to steel moment frames. *Earthquake Engineering & Structural Dynamics*, *52*(8), 2339–2359. https://doi.org/10.1002/eqe.3810

Federal Emergency Management Agency (FEMA P-259). (2012). *Engineering principles and practices for retrofitting flood-prone residential structures*. Federal Emergency Management Agency (FEMA).

Federal Emergency Management Agency (FEMA P695). (2009). *Quantification of building seismic performance factors*. Federal Emergency Management Agency (FEMA). US Department of Homeland Security.

Federal Emergency Management Agency (FEMA P58-1). (2012). *Seismic performance assessment of buildings volume 1-methodology*. Federal Emergency Management Agency (FEMA).

Federal Emergency Management Agency (FEMA). (2014). *Guidance for flood risk analysis and mapping: Flood depth and analysis grids*. Author.

Ge, B., Yang, Y., & Kim, S. (2023). Time-dependent multi-hazard seismic vulnerability and risk assessment of deteriorating reinforced concrete bridges considering climate change. *Structures*, *55*, 995–1010. https://doi.org/10.1016/j.istruc.2023.06.068

Ghaffarpasand, B., Samadian, D., Raissi Dehkordi, M., Bocchini, P., & Eghbali, M. (2024). Investigation of different resilience-based optimisation strategies for retrofitting curved bridges. *Structure and Infrastructure Engineering*, *20*(12), 1925–1939. https://doi.org/10.1080/15732479.2023.2165690

Guan, X. (2021). *Performance-based analytics-driven seismic design of steel moment frame buildings* [Doctoral dissertation]. University of California Los Angeles. University of California Los Angeles Theses and Dissertations Archive. https://escholarship.org/uc/item/5bd6r600

Guha-Sapir, D., D'Aoust, O., & Hoyois, P. (2013). The frequency and impact of natural disasters. In D. Guha-Sapir, I. Santos, & A. Borde (Eds.), *The economics of natural disasters* (pp. 7–27). Oxford University Press. https://doi.org/10.1093/acprof:Oso/9780199841936.003.0002

Guo, X., Wu, Y., & Guo, Y. (2016). Time-dependent seismic fragility analysis of bridge systems under scour hazard and earthquake loads. *Engineering Structures*, *121*, 52–60. https://doi.org/10.1016/j.engstruct.2016.04.038

Harati, M., & van de Lindt, J. W. (2024). Methodology to generate earthquake-tsunami fragility surfaces for community resilience modeling. *Engineering Structures*, *305*, 117700. https://doi.org/10.1016/j.engstruct.2024.117700

Hsiao, J. K., Schultz, W., Petersen, T., & Vaicik, S. (2008). Computation of story drifts considering panel zone deformations for multistory steel moment frames with welded flange plate connections. *The Structural Design of Tall and Special Buildings*, *17*(2), 419–443. https://doi.org/10.1002/tal.362

Ibarra, L., Ricardo, F., Medina, A., & Krawinkler, H. (2005). Hysteretic models that incorporate strength and stiffness deterioration. *Earthquake Engineering & Structural Dynamics*, *34*(12), 1489–1511. https://doi.org/10.1002/eqe.495

Jasak, H. (2009). OpenFOAM: Open source CFD in research and industry. *International Journal of Naval Architecture and Ocean Engineering*, *1*(2), 89–94. https://doi.org/10.2478/IJNAOE-2013-0011

Jones, L. M. (2019). *The big ones: How natural disasters have shaped us (and what we can do about them)*. Anchor Books.

Jonkman, S. N., Curran, A., & Bouwer, L. M. (2024). Floods have become less deadly: An analysis of global flood fatalities 1975–2022. *Natural Hazards*, *120*(7), 6327–6342. https://doi.org/10.1007/s11069-024-06444-0

Jonkman, S. N., & Vrijling, J. K. (2008). Loss of life due to floods. *Journal of Flood Risk Management*, *1*(1), 43–56. https://doi.org/10.1111/j.1753-318X.2008.00006.x

Kelman, I. (2022). *Physical flood vulnerability of residential properties in coastal, Eastern England* [Doctoral dissertation]. University of Cambridge. Retrieved from https://ilankelman.org/phd/IlanKelmanPhDDissertation.pdf

Kim, T., & Han, S. W. (2021). Seismic collapse performance of steel special moment frames designed using different analysis methods. *Earthquake Spectra*, *37*(2), 988–1012. https://doi.org/10.1177/8755293020970969

Korswagen, P. A., Jonkman, S. N., & Terwel, K. C. (2019). Probabilistic assessment of structural damage from coupled multi-hazards. *Structural Safety*, *76*, 135–148. https://doi.org/10.1016/j.strusafe.2018.08.001

Kreibich, H., Van Loon, A. F., Schröter, K., Ward, P. J., Mazzoleni, M., Sairam, N., Abeshu, G. W., Agafonova, S., AghaKouchak, A., Aksoy, H., Alvarez-Garreton, C., Aznar, B., Balkhi, L., Barendrecht, M. H., Biancamaria, S., Bos-Burgering, L., Bradley, C., Budiyono, Y., Buytaert, W., Capewell, L., Carlson, H., Cavus, Y., Couasnon, A.,

Coxon, G., Daliakopoulos, I., de Ruiter, M. C., Delus, C., Erfurt, M., Esposito, G., François, D., Frappart, F., Freer, J., Frolova, N., Gain, A. K., Grillakis, M., Grima, J. O., Guzmán, D. A., Huning, L. S., Ionita, M., Kharlamov, M., Khoi, D. N., Kieboom, N., Kireeva, M., Koutroulis, A., Lavado-Casimiro, W., Li, H.-Y., LLasat, M. C., Macdonald, D., Mård, J., Mathew-Richards, H., McKenzie, A., Mejia, A., Mendiondo, E. M., Mens, M., Mobini, S., Mohor, G. S., Nagavciuc, V., Ngo-Duc, T., Thao Nguyen Huynh, T., Nhi, P. T. T., Petrucci, O., Nguyen, H. Q., Quintana-Seguí, P., Razavi, S., Ridolfi, E., Riegel, J., Sadik, M. S., Savelli, E., Sazonov, A., Sharma, S., Sörensen, J., Arguello Souza, F. A., Stahl, K., Steinhausen, M., Stoelzle, M., Szalińska, W., Tang, Q., Tian, F., Tokarczyk, T., Tovar, C., Tran, T. V. T., Van Huijgevoort, M. H. J., van Vliet, M. T. H., Vorogushyn, S., Wagener, T., Wang, Y., Wendt, D. E., Wickham, E., Yang, L., Zambrano-Bigiarini, M., Blöschl, G., & Di Baldassarre, G. (2022). The challenge of unprecedented floods and droughts in risk management. *Nature*, *608*(7921), 80–86. https://doi.org/10.1038/s41586-022-04917-5

Los Angeles County Department of Public Works (LACDPW). (2024). *Levee Certification Program*. Retrieved from https://dpw.lacounty.gov/wmd/nfip/dsp_LeveeCertificationFAQs.aspx

Le, T. T. H., Nguyen, V. C., Nguyen, D. T., & Tran, D. T. (2024). Coupling CFD model and FEM model to investigate the impact of debris flows on a low-rise building. *Results in Engineering*, *24*, 103063. https://doi.org/10.1016/j.rineng.2024.103063

Lignos, D. G., & Krawinkler, H. (2007). A database in support of modeling of component deterioration for collapse prediction of steel frame structures. *Structural Engineering Research Frontiers*, *137*(11), 1–12. https://doi.org/10.1061/40944(249)3

Lignos, D. G., & Krawinkler, H. (2011). Deterioration modeling of steel components in support of collapse prediction of steel moment frames under earthquake loading. *Journal of Structural Engineering*, *137*(11), 1291–1302. https://doi.org/10.1061/(ASCE)ST.1943-541X.0000376

Lignos, D. G., Putman, C., & Krawinkler, H. (2013). Seismic assessment of steel moment frames using simplified nonlinear models. In M. Papadrakakis, M. Fragiadakis, & V. Plevris (Eds.), *Computational methods in earthquake engineering. Computational methods in applied sciences* (Vol. 30, pp. 91–109). Springer. https://doi.org/10.1007/978-94-007-6573-3_5

Liu, J., Zhai, C., & Yu, P. (2022). A probabilistic framework to evaluate seismic resilience of hospital buildings using Bayesian networks. *Reliability Engineering & System Safety*, *226*, 108644. https://doi.org/10.1016/j.ress.2022.108644

Lonetti, P., & Maletta, R. (2018). Dynamic impact analysis of masonry buildings subjected to flood actions. *Engineering Structures*, *167*, 445–458. https://doi.org/10.1016/j.engstruct.2018.03.076

Mazzorana, B., Simoni, S., Scherer, C., Gems, B., Fuchs, S., & Keiler, M. (2014). A physical approach on flood risk vulnerability of buildings. *Hydrology and Earth System Sciences*, *18*(9), 3817–3836. https://doi.org/10.5194/hess-18-3817-2014

Milanesi, L., Pilotti, M., Belleri, A., Marini, A., & Fuchs, S. (2018). Vulnerability to flash floods: A simplified structural model for masonry buildings. *Water Resources Research*, *54*(10), 7177–7197. https://doi.org/10.1029/2018WR022577

Motley, M. R., Wong, H. K., Qin, X., Winter, A. O., & Eberhard, M. O. (2016). Tsunami-induced forces on skewed bridges. *Journal of Waterway, Port, Coastal, and Ocean Engineering*, *142*(3), 04015025. https://doi.org/10.1061/(ASCE)WW.1943-5460.0000328

National Institute of Standards and Technology (NIST). (2010). *Evaluation of the FEMA P-695 methodology for quantification of building seismic performance factors* (Report No. NIST GCR 10-917-8). US National Institute of Standards and Technology (NIST) by the NEHRP Consultants Joint Venture.

Petrone, C., Rossetto, T., Baiguera, M., Barra, C., De. la, B., & Ioannou, I. (2020). Fragility functions for a reinforced concrete structure subjected to earthquake and tsunami in sequence. *Engineering Structures*, *205*, 110120. https://doi.org/10.1016/j.engstruct.2019.110120

Prasad, G. G., & Banerjee, S. (2013). The impact of flood-induced scour on seismic fragility characteristics of bridges. *Journal of Earthquake Engineering*, *17*(6), 803–828. https://doi.org/10.1080/13632469.2013.771593

Pregnolato, M., Winter, A. O., Mascarenas, D., Sen, A. D., Bates, P., & Motley, M. R. (2022). Assessing flooding impact to riverine bridges: An integrated analysis. *Natural Hazards and Earth System Sciences*, *22*(5), 1559–1576. https://doi.org/10.5194/nhess-22-1559-2022

Prendergast, L. J., Limongelli, M. P., Ademovic, N., Anžlin, A., Gavin, K., & Zanini, M. (2018). Structural health monitoring for performance assessment of bridges under flooding and seismic actions. *Structural Engineering International*, *28*(3), 296–307. https://doi.org/10.1080/10168664.2018.1472534

Samadian, D., Ghafory-Ashtiany, M., Naderpour, H., & Eghbali, M. (2019). Seismic resilience evaluation based on vulnerability curves for existing and retrofitted typical RC school buildings. *Soil Dynamics and Earthquake Engineering*, *127*, 105844. https://doi.org/10.1016/j.soildyn.2019.105844

Samadian, D., Fayaz, J., Muhit, I. B., & Dawood, N. (2024). Structural failure analysis with CMS-based ground motion selection using innovative cost function and weight factors. *Earthquake Engineering and Engineering Vibration*, *23*(4), 899–918. https://doi.org/10.1007/s11803-024-2279-z

Samadian, D., Fayaz, J., Muhit, I. B., Occhipinti, A., & Dawood, N. (2024). Meta databases of steel frame buildings for surrogate modelling and machine learning-based feature importance analysis. *Resilient Cities and Structures*, *3*(1), 20–43. https://doi.org/10.1016/j.rcns.2023.12.001

Samadian, D., Muhit, I. B., Occhipinti, A., Fayaz, J., & Dawood, N. (2024). Surrogate models for seismic and pushover response prediction of steel special moment resisting frames. *Engineering Structures*, *314*, 118307. https://doi.org/10.1016/j.engstruct.2024.118307

Sanders, B. F., Schubert, J. E., Kahl, D. T., Mach, K. J., Brady, D., AghaKouchak, A., Forman, F., Matthew, R. A., Ulibarri, N., & Davis, S. J. (2022). Large and inequitable flood risks in Los Angeles, California. *Nature Sustainability*, *6*(1), 47–57. https://doi.org/10.1038/s41893-022-00977-7

Soltani, M., Raissi Dehkordi, M., Eghbali, M., Samadian, D., & Salmanmohajer, H. (2023). Influence of infill walls on resilience index of RC schools using the BIM analysis and FEMA P-58 methodology. *International Journal of Civil Engineering*, *21*(5), 711–726. https://doi.org/10.1007/s40999-022-00777-2

Tagle, S. J., Jünemann, R., Vásquez, J., de la Llera, J. C., & Baiguera, M. (2021). Performance of a reinforced concrete wall building subjected to sequential earthquake and tsunami loading. *Engineering Structures*, *238*, 111995. https://doi.org/10.1016/j.engstruct.2021.111995

Torres-Rodas, P., Flores, F., Pozo, S., & Astudillo, B. X. (2021). Seismic performance of steel moment frames considering the effects of column-base hysteretic behavior and gravity framing system. *Soil Dynamics and Earthquake Engineering*, *144*, 106654. https://doi.org/10.1016/j.soildyn.2021.106654

UCIrvine News (2022). *UCI flood modeling framework reveals heightened risk and disparities in Los Angeles*. https://news.uci.edu/2022/10/31/uci-flood-modeling-framework-reveals-heightened-risk-and-disparities-in-los-angeles/

United Nations Office for Disaster Risk Reduction (UNDRR). (2015, March 14–18). *Sendai framework for disaster risk reduction* [Paper presentation]. Proceedings of the 3rd United Nations World Conference on Disaster Risk Reduction (WCDRR), Sendai, Japan (pp. 14–18).

U.S. Army Corps of Engineers (USACE). (2011). *Engineering and design, safety of dams—Policy and procedures*. https://planning.erdc.dren.mil/toolbox/library/ERs/ER1100_2_1156_28Oct11.pdf

U.S. Army Corps of Engineers (USACE). (2016). *Hydraulics report. Floodplain analysis, Los Angeles River: Barham Boulevard to First Street*. Flood Plain Management Services Special Study. https://eng2.lacity.org/projects/LARIVER_Glendale_Narrows/docs/LAR_FPMS_Hydraulic_Report_FINAL_October2016_CompleteDocument.pdf

U.S. Army Corps of Engineers (USACE). (2022). *Levee Safety Program. Inspection summaries for the Los Angeles River, San Gabriel River,*

Rio Hondo Channel, and Compton Creek. https://www.spl.usace.army.mil/Missions/Civil-Works/Levee-Safety-Program

Vanneste, K., Camelbeeck, T., Verbeeck, K., & Demoulin, A. (2018). Morphotectonics and past large earthquakes in eastern Belgium. In A. Demoulin (Ed.), *Landscapes and landforms of Belgium and Luxembourg. World geomorphological landscapes* (pp. 215–236). Springer. https://doi.org/10.1007/978-3-319-58239-9_13

Vatteri, A. P., D'Ayala, D., & Gehl, P. (2022). Bayesian networks for assessment of disruption to school systems under combined hazards. *International Journal of Disaster Risk Reduction*, *74*, 102924. https://doi.org/10.1016/j.ijdrr.2022.102924

Viccione, G., & Izzo, C. (2022). Three-dimensional CFD modelling of urban flood forces on buildings: A case study. *Journal of Physics: Conference Series*, *2162*(1), 012020. https://doi.org/10.1088/1742-6596/2162/1/012020

Wang, Z., Dueñas-Osorio, L., & Padgett, J. E. (2014). Influence of scour effects on the seismic response of reinforced concrete bridges. *Engineering Structures*, *76*, 202–214. https://doi.org/10.1016/j.engstruct.2014.06.026

Wang, S., Lai, J.-W., Schoettler, M. J., & Mahin, S. A. (2017). Seismic assessment of existing tall buildings: A case study of a 35-story steel building with pre-Northridge connection. *Engineering Structures*, *141*, 624–633. https://doi.org/10.1016/j.engstruct.2017.03.047

Wieser, J. (2011). *Assessment of floor accelerations in yielding buildings* [Master's thesis]. University of Nevada, Reno. University of Nevada e-Thesis Repository. https://www.buffalo.edu/mceer/catalog.host.html/content/shared/www/mceer/publications/MCEER-12-0008.detail.html

Winter, A. O., Motley, M. R., & Eberhard, M. O. (2018). Tsunami-like wave loading of individual bridge components. *Journal of Bridge Engineering*, *23*(2), 04017137. https://doi.org/10.1061/(ASCE)BE.1943-5592.0001177

World Economic Forum. (2023). *The global risks report* (18th ed.). https://www.weforum.org/publications/global-risks-report-2023/

Xu, J. G., Wu, G., Feng, D. C., & Fan, J. J. (2021). Probabilistic multi-hazard fragility analysis of RC bridges under earthquake-tsunami sequential events. *Engineering Structures*, *238*, 112250. https://doi.org/10.1016/j.engstruct.2021.112250

Xu, D., Xie, Q., & Hao, W. (2024). Seismic damage evaluation of historical masonry towers through numerical model. *Bulletin of Earthquake Engineering*, *22*(4), 2235–2266. https://doi.org/10.1007/s10518-024-01858-4

Zareian, F., Lignos, D. G., & Krawinkler, H. (2010). Evaluation of seismic collapse performance of steel special moment resisting frames using FEMA P695 (ATC-63) methodology. In *Proceedings of Structures Congress* (pp. 1275–1286). American Society of Civil Engineers. https://doi.org/10.1061/41130(369)11

Zhu, M., McKenna, F., & Scott, M. H. (2018). OpenSeesPy: Python library for the OpenSees finite element framework. *SoftwareX*, *7*, 6–11. https://doi.org/10.1016/j.softx.2017.10.009